NAVAL POSTGRADUATE SCHOOL

MONTEREY, CALIFORNIA

THESIS

SUAS-BASED PAYLOAD DEVELOPMENT AND TESTING FOR QUANTIFYING OPTICAL TURBULENCE

by

Lee Suring
June 2018

Thesis Advisor: Qing Wang
Co-Advisor: Kevin D. Jones

Approved for public release. Distribution is unlimited.

THIS PAGE INTENTIONALLY LEFT BLANK

REPORT DOCUMENTATION PAGE	*Form Approved OMB No. 0704-0188*

1. AGENCY USE ONLY *(Leave blank)*	**2. REPORT DATE** June 2018	**3. REPORT TYPE AND DATES COVERED** Master's thesis

4. TITLE AND SUBTITLE SUAS-BASED PAYLOAD DEVELOPMENT AND TESTING FOR QUANTIFYING OPTICAL TURBULENCE	**5. FUNDING NUMBERS** RLM6R
6. AUTHOR(S) Lee Suring	
7. PERFORMING ORGANIZATION NAME(S) AND ADDRESS(ES) Naval Postgraduate School Monterey, CA 93943-5000	**8. PERFORMING ORGANIZATION REPORT NUMBER**
9. SPONSORING / MONITORING AGENCY NAME(S) AND ADDRESS(ES) N/A	**10. SPONSORING / MONITORING AGENCY REPORT NUMBER**

11. SUPPLEMENTARY NOTES The views expressed in this thesis are those of the author and do not reflect the official policy or position of the Department of Defense or the U.S. Government.

12a. DISTRIBUTION / AVAILABILITY STATEMENT Approved for public release. Distribution is unlimited.	**12b. DISTRIBUTION CODE** A

13. ABSTRACT (maximum 200 words)

High Energy Laser (HEL) systems are becoming ubiquitous across the Department of Defense for their precision, low shot cost, tunability and cycling time. However, laser propagation through the atmosphere is affected by atmospheric turbulence. It is essential to quantify this atmospheric effect to predict operational conditions as well as improve laser system performance. The main objective of this study is to quantity optical turbulence within the atmospheric boundary layer using a small Unmanned Aircraft System (sUAS). The sUAS-based sensor package was developed for this application. Temperature and humidity profiles were derived from a radiosonde system onboard the sUAS. Additionally, high-rate temperature and slow-response temperature were measured by a thermocouple and a high-accuracy platinum thermometer, respectively. All of these meteorological components were integrated into a comprehensive, lightweight and low-power consumption sUAS payload system. The sensor package was thoroughly ground tested in comparison with proven methods. Test flights of the sensor package integrated onto the sUAS were made at the McMillian Airfield. The platform proved itself in flying at various altitudes within the surface layer to measure optical turbulence. Optical turbulence varied most directly near the surface as a result of strong surface buoyancy forcing. Results of the mean profiles as well as optical turbulence from test flights and comparison bench testing are discussed.

14. SUBJECT TERMS sUAS, thermocouple, boundary layer, turbulence, ct2, cn2, electro-optical, scintillation, Penguin, high energy laser, lower atmosphere	**15. NUMBER OF PAGES** 83
	16. PRICE CODE

17. SECURITY CLASSIFICATION OF REPORT	**18. SECURITY CLASSIFICATION OF THIS PAGE**	**19. SECURITY CLASSIFICATION OF ABSTRACT**	**20. LIMITATION OF ABSTRACT**
Unclassified	Unclassified	Unclassified	UU

NSN 7540-01-280-5500 Standard Form 298 (Rev. 2-89) Prescribed by ANSI Std. 239-18

THIS PAGE INTENTIONALLY LEFT BLANK

Approved for public release. Distribution is unlimited.

SUAS-BASED PAYLOAD DEVELOPMENT AND TESTING FOR QUANTIFYING OPTICAL TURBULENCE

Lee Suring
Lieutenant, United States Navy
BSME, University of Arizona, 2012

Submitted in partial fulfillment of the
requirements for the degree of

MASTER OF SCIENCE IN METEOROLOGY AND PHYSICAL OCEANOGRAPHY

from the

NAVAL POSTGRADUATE SCHOOL
June 2018

Approved by: Qing Wang
Advisor

Kevin D. Jones
Co-Advisor

Wendell A. Nuss
Chair, Department of Meteorology

THIS PAGE INTENTIONALLY LEFT BLANK

ABSTRACT

High Energy Laser (HEL) systems are becoming ubiquitous across the Department of Defense for their precision, low shot cost, tunability and cycling time. However, laser propagation through the atmosphere is affected by atmospheric turbulence. It is essential to quantify this atmospheric effect to predict operational conditions as well as improve laser system performance. The main objective of this study is to quantity optical turbulence within the atmospheric boundary layer using a small Unmanned Aircraft System (sUAS). The sUAS-based sensor package was developed for this application. Temperature and humidity profiles were derived from a radiosonde system onboard the sUAS. Additionally, high-rate temperature and slow-response temperature were measured by a thermocouple and a high-accuracy platinum thermometer, respectively. All of these meteorological components were integrated into a comprehensive, lightweight and low-power consumption sUAS payload system. The sensor package was thoroughly ground tested in comparison with proven methods. Test flights of the sensor package integrated onto the sUAS were made at the McMillian Airfield. The platform proved itself in flying at various altitudes within the surface layer to measure optical turbulence. Optical turbulence varied most directly near the surface as a result of strong surface buoyancy forcing. Results of the mean profiles as well as optical turbulence from test flights and comparison bench testing are discussed.

THIS PAGE INTENTIONALLY LEFT BLANK

TABLE OF CONTENTS

THIS PAGE INTENTIONALLY LEFT BLANK

LIST OF FIGURES

THIS PAGE INTENTIONALLY LEFT BLANK

LIST OF TABLES

THIS PAGE INTENTIONALLY LEFT BLANK

LIST OF ACRONYMS AND ABBREVIATIONS

AGL	above ground level
DoD	Department of Defense
ECE	energy-containing eddies
FPV	first-person-viewpoint
GCS	ground control system (GCS)
HEL	high energy laser
HELCAP	High Energy Laser Code for Atmospheric Propagation (HELCAP)
HELEEOS	High Energy Laser End-to-End Operational Simulation
JIFX	Joint Interagency Field Experimentation
IRGASON	InfraRed Gas Analyzer SONic anemometer
LaWS	laser weapon system
LOS	line of sight
MOS	Monin-Obukhov Similarity
MSL	mean sea level
NAVSLaM	Navy Atmospheric Vertical Surface Layer Model
NRL	Naval Research Laboratory
OTS	optical turbulence sensing
RC	remote control
RTD	resistance temperature detector
SHiELD	Self-protect High Energy Laser Demonstrator
sUAS	small unmanned aerial system
TKE	turbulent kinetic energy
UAV	unmanned aerial vehicles
VLOS	visual line of sight

THIS PAGE INTENTIONALLY LEFT BLANK

I. INTRODUCTION

A. OVERVIEW

Within the highly dynamic and hostile modern day battlespace, the Department of Defense (DoD) is constantly facing threats from multiple domains. Unmanned aerial vehicles (UAV), swarms of fast attack craft, anti-ship missiles and manned aircraft are quickly developing asymmetric options. These threats need to be tracked, engaged and destroyed in quick succession. However, not all threats can necessarily be paired with the same weapons system.

The use of directed electro-optical energy has a long history in warfare dating back to the days of the Romans. According to legend, Archimedes used an array of mirrors to direct beams of sunlight on enemy ships to burn them down before they could invade Syracuse. In more recent times, the Navy began experimenting with the use of chemical lasers in the 1970s. Unfortunately, these early attempts were only experimental and never were put into operational use. Their size was too vast to be employed on ships, vehicles or aircraft. Over time however, as laser technology improved and shifted from chemical lasers to solid state, their size diminished. They are beginning to become employable on several DoD assets. Currently, the Navy uses many different weapons platforms including the Phalanx CIWS, M242 Bushmaster cannon and BAE Systems Mk 45 5 in gun to neutralize symmetric threats. To complement these weapons platforms, the Navy is developing the AN/SEQ-3 laser weapon system (or XN-1 LaWS). In other forces of the DoD, the Army conducted a test of a high energy laser (HEL) systems onboard an AH-64 Apache attack helicopter and the Air Force is forging ahead with their self-protect high energy laser demonstrator (SHiELD) program which they hope will help to defend its fighter planes.

There are many benefits of adding a laser system to the current array of defenses. Some of these include target cycling time, low shot cost, and tunability. Targets can be taken out in quick succession as each shot only requires a matter of seconds before targeting the next object. The shot is received by the target instantaneously and can be

essential for fast moving, inbound targets. Each shot of the laser only requires about a dollar of energy since it is the only "projectile" involved. With the laser system, there is no required storage, disposal, purchase, transport or development of ordnance. Many of the projectiles of the systems mentioned earlier cost hundreds upwards of hundreds of thousands of dollars for every target they engage. Handling the ordnance takes up tight space aboard the ships and maintaining the stockpile is a continuous cycle. Finally, lasers can be tuned in at high enough power levels to vaporize incoming howitzer shells or to docile enough levels enough to simply disable optical sensors onboard a UAV, all within the same system.

Unfortunately, despite all the benefits of laser systems, they can be disrupted by atmospheric conditions, over land and over the ocean. The atmosphere is a continually changing mixture of aerosols (dust, salts, etc.) and radiatively active gases such as carbon dioxide and water vapor. Each of these constituents have a direct effect on laser propagation through scattering, refraction and absorption. In addition to these effects, atmospheric turbulence on very small scales (centimeter to meter), can cause atmospheric scintillation which affects the spreading and coherence of electro-optical propagation. The better we can understand these effects and the makeup of the atmosphere within the battlespace, the more precisely we can predict and mitigate the atmospheric effects of HEL systems. Currently, most atmospheric models work at grid scales of 2 km or greater which are unable to resolve these critical components. Unlike missile and gun-based defense systems which can be projected over the horizon, laser systems are restricted to line-of-sight firing.

B. OBJECTIVES OF THE THESIS

The objective of this thesis is to explore the use of small unmanned aerial systems (sUAS) to measure turbulence within the boundary layer to help predict the atmospheric effects on laser propagation. The sUASs platform is especially versatile in comparison to their manned fixed wing counterparts in that they can fly within 15 meters of the surface. Close to the ground is generally where turbulence is most severe due to land/sea-air interaction. Additionally, sUAS are especially adept at quickly flying a diagonal profile

from near the surface to the top of the boundary layer to obtain a vertical gradient of turbulence or other atmospheric variables. This gives the user the ability to survey the air parcel from laser system to target which actually affects propagation.

Collecting this data will help validate and develop models of the turbulence within the boundary layer at a more intricate scale. The lack of data available to help refine models is a major hindrance to model evaluation and improvement. Currently, data collection above ground level is difficult due to the reasons discussed earlier with manned flight platforms, as well as ground-based tower setups. Unfortunately, environmental propagation effects have strong spatial and temporal variations which make them notoriously difficult to model.

C. STRUCTURE OF THE THESIS

This thesis is organized as follows. An introduction into the DoD's interest in HEL weapons with their advantages and limitations is given in Chapter I. It also explores atmospheric impacts which affect HEL weapons. These atmospheric impacts are discussed on a deeper level while also exploring models for optical turbulence and system performance in Chapter II. Additionally, investigation into sUAS-based measurements for quantifying the lower atmosphere are discussed in Chapter II. The sUAS with its optical turbulence sensing (OTS) payload as well as ground testing and data collection flights conducted is introduced in Chapter III. Results from the newly developed sensing system on the sUAS is presented in Chapter IV. Summary and conclusions are given in Chapter V.

THIS PAGE INTENTIONALLY LEFT BLANK

II. BACKGROUND

A. OPTICAL PROPAGATION

Optical propagation through the atmosphere can be significantly affected by various atmospheric variables along the laser's path at a given time. Among these variables are aerosols and atmospheric turbulence resulting in small variations of the refractive index (Andrews, 2004). Both are most abundant in the atmospheric boundary layers. Aerosols are small particulates suspended in the air. They affect optical propagation through absorption and scattering of the laser beam. Aerosol characteristics, including their number concentration, size, shape, and composition, can significantly modify their effects on scattering and absorption and hence the propagation of the HEL beam. Aerosol evolution can be also impacted by the amount of water vapor in the atmosphere. Temperature perturbations in a turbulent environment, are a major concern for the beam quality of the HEL weapons. Water vapor perturbations are significant, although to a lesser extent than temperature perturbations. Their combined effect is referred to as scintillation.

The American Meteorological Society Glossary of Meteorology defines the atmospheric boundary layer as "the bottom layer of the troposphere that is in contact with the surface of the earth. It is often turbulent and is capped by a statically stable layer of air" (Stull, 2018). Aerosol concentration and compositions, as well as turbulence in the atmospheric boundary layer, can change rapidly within mere kilometers and hours. For many HEL applications, the laser emitter and/or the targets they encounter likely reside close to the surface. Hence, it is important to understand and predict the thermodynamics, aerosol, and turbulence properties in the atmospheric boundary layers.

B. SCINTILLATION

Scintillation refers to the variations in the apparent brightness of a light source illuminating a target. This is generally an effect of fluctuations in the atmospheric refractive index as a result of turbulence. Our objective here is to discuss scintillation and how it affects electro-optical, particularly HEL, propagation. Scintillation effects are seen

in HEL as rapid variations in the energy density over a given area as the laser strikes a target, similar to the twinkle of a star's light as it approaches our eyes through the atmosphere. An example of the difference in a laser's power distribution upon a target with and without the effects of turbulence is given in Figure 1.

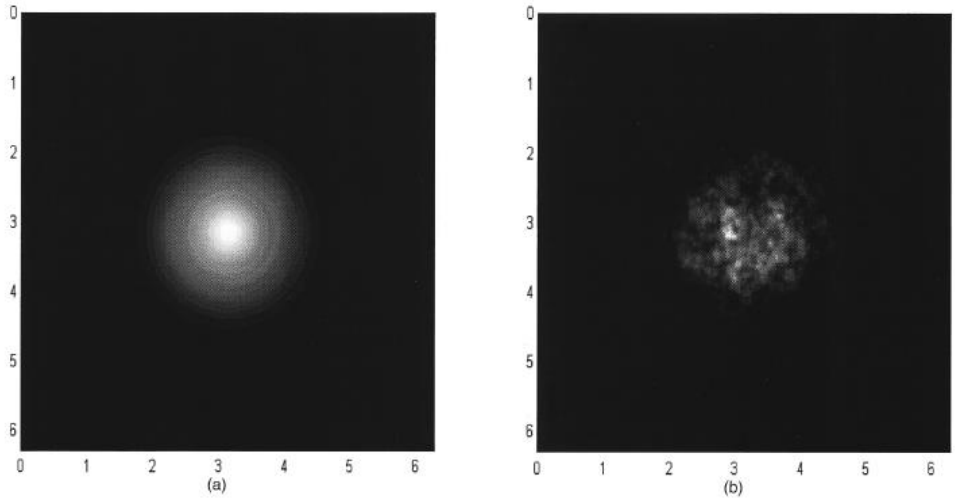

"Computer images of a 10.6-μm Gaussian beam intensity on target. Propagation distance is 7300 m and the diffraction-limited beam divergence is 0.290 mrad. Axis values are in meters. The simulation used 10 propagation steps of 730 m each with a 512 × 512 array: (a) with zero turbulence and (b) a uniform turbulence level of $C_n^2 = 10^{-14}$ $m^{-2/3}$. The modeled beam path is horizontal and ~3 m above the ground" Nelson (2000).

Figure 1. Effect of scintillation on a laser's power distribution. Source: Nelson (2000).

Scintillation effects are derived from variations in the refractive index of air parcels within the atmosphere. The refractive index of light is a measure of its speed in a given medium as compared to its speed in a vacuum. It is defined in Equation (1) as *n*, where *c* is the speed of light in a vacuum and *v* is the phase velocity within the medium.

$$n = \frac{c}{v} \tag{1}$$

The refractive index of the atmosphere can be expressed in terms of thermodynamic variables such as temperature (*T*), pressure (*P*), and specific humidity (*q*) as shown in Equation (2) (Fredrickson, 2000):

$$n = 1 + 10^{-6}\{m_1(\lambda)\frac{P}{T} + [m_2(\lambda) - m_1(\lambda)]\frac{qP}{T\varepsilon\gamma}\} \tag{2}$$

Here, λ is the wavelength in micron (μm), ε is the ratio of ideal gas constants of dry air and water vapor, and $\gamma = 1 + 0.608q$. The m_1 and m_2 functions in Equation (2) are further defined in Equation (3):

$$m_1(\lambda) = 23.7134 + \frac{6839.397}{130 - \lambda^{-2}} + \frac{45.473}{38.9 - \lambda^{-2}} \tag{3}$$

$$m_2(\lambda) = 64.8731 + 0.58058\lambda^{-2} - 0.0071150\lambda^{-4} + 0.0008851\lambda^{-6}$$

The spatial variation of n is critical to the path of the light beam as described by Snell's law. The change of beam direction as light passes between two mediums of different indices of refractivity is illustrated in Figure 2. The outgoing light's angle can change from its incoming angle as the light either slows down or speeds up within the new medium. Snell's law describes this relationship in Equation (4):

$$\frac{\sin\theta_2}{\sin\theta_1} = \frac{v_2}{v_1} = \frac{n_1}{n_2} \tag{4}$$

Where θ_1 and θ_2 are the incident and outgoing angles, respectively. The subscript "1" and "2" denote medium 1 and 2, respectively.

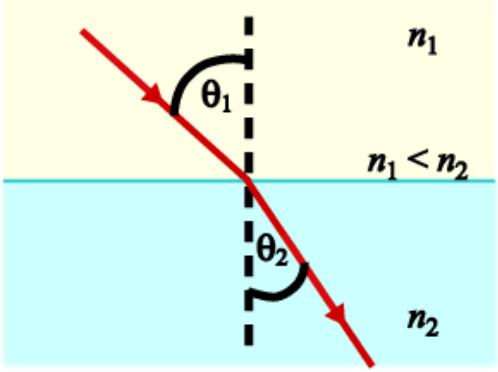

Note the change of propagation direction in two media with different indices of refraction.

Figure 2. An illustration of the Snell's law. Source: Wagner (1999).

The refractive index in the atmosphere changes primarily due to temperature perturbations. These variations can occur on a scale of centimeters to kilometers, leading to variations of *n* on various scales over a path length. As light passes through a series of these refractivity modifications, it changes the wave front of propagation from its original direction and homogeneity to produce the phenomenon of scintillation as illustrated in Figure 3.

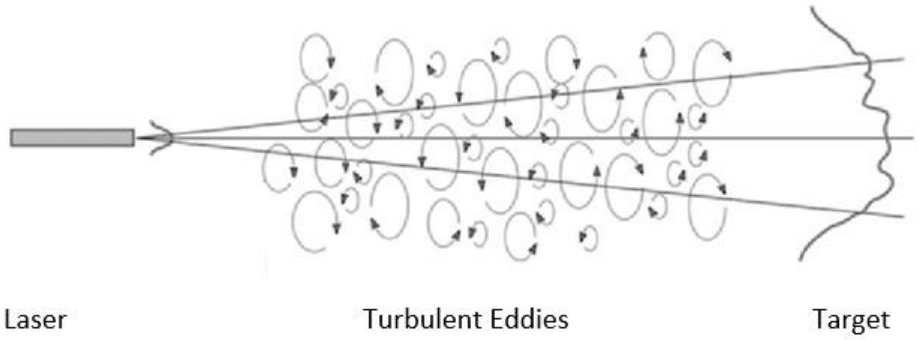

Figure 3. An illustration of wave front deformation as the laser beam passes through a turbulent medium. Adapted from Burger, Litvin, and Forbes (2008).

To characterize the significance of these refractivity modifications, it is important to understand the size of the eddies important to optical propagation. The turbulence

energy cascade describes a continuous energy drop from energy-containing eddies (ECE) to the smallest dissipation eddies. The large energy-containing eddies can be caused by buoyancy as well as wind shear. The smallest eddies dissipate turbulent kinetic energy (TKE) into heating the medium. The size range between the ECE and the dissipation eddies is usually referred to as the inertial subrange. Eddies in this range are of the most interest to optical propagation. Turbulence theory and measurements have demonstrated that the energy density spectra in the inertial subrange follows a -5/3 relationship with frequency as seen in Figure 4. Due to the nature of turbulence, the effects of the individual eddies need to be described statistically.

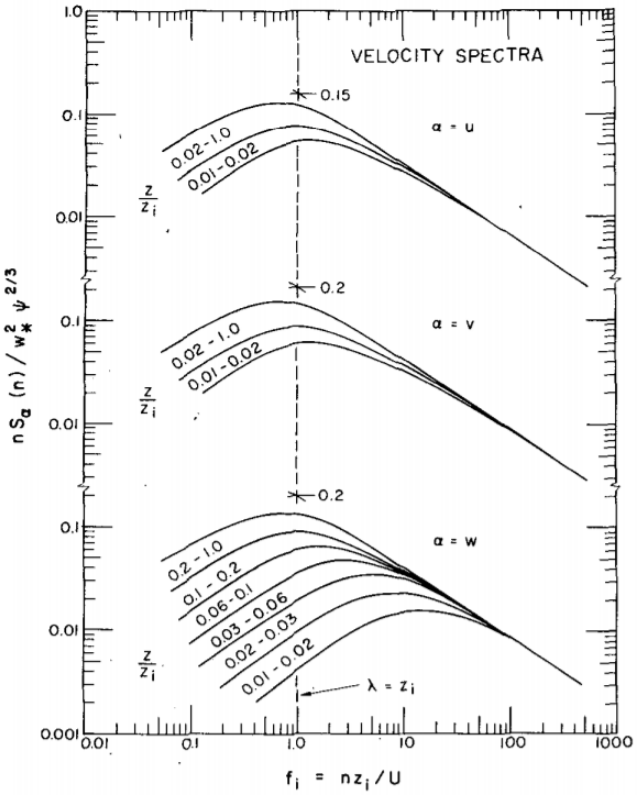

"Universal curves for velocity spectra expressed in mixed layer similarity coordinates. The function Ψ in the spectral normalization is the dimensionless energy dissipation rate $\varepsilon/(g/T)Q_0$" Kaimal et al. (1976).

Figure 4. An example of the energy density spectra in the inertial subrange following a -5/3 relationship with frequency.
Source: Kaimal et al. (1976).

C. TURBULENCE STRUCTURE PARAMETER

The turbulence structure function, defined on the left-hand-side of Equation (5), is a statistical quantity that best describes the atmospheric turbulent variabilities affecting the propagation of electromagnetic radiation through a turbulent medium (Tatarskii, 1971).

$$< [n'(x) - n'(x+r)]^2 >= C_n^2 r^{-2/3} \tag{5}$$

Here, *n'(x)* and *n'(x+r)* define index of refraction perturbations at two points within a medium with a distance of *r* between the two. The angular bracket represents the ensemble average of this difference.

The turbulence structure parameter (C_n^2) can be derived from the structure function based on Equation (5) following Kolmogorov's turbulence theory stating that the structure parameter is a proportionality factor in the 2/3-law for the structure function. This parameter is normally used to describe the statistical effect of the turbulent medium on the quality of optical transmission due to the various eddy sizes. Transmission quality degradation is hence due to these inhomogeneities in the atmosphere's refractive index.

Since the index of refraction is a function of atmospheric parameters such as temperature and humidity, it follows that C_n^2 should be expressed in terms of these parameters as well. Like the structure function parameter for *n*, one can define the structure parameter for other variables such as temperature, water vapor specific humidity, and the cross-correlation between the two as given in Equations (6-8).

$$< T'(x) - T'(x+r) >^2 = C_T^2 r^{-2/3} \tag{6}$$

$$< q'(x) - q'(x+r) >^2 = C_q^2 r^{-2/3} \tag{7}$$

$$< T'(x) - T'(x+r) >< q'(x) - q'(x+r) >= C_{Tq} r^{-2/3} \tag{8}$$

Following Equations (1) and (5) for the definitions of index of refraction and its structure parameter, Andreas (1987) and Fredrickson (2000), related the refractive index

structure parameter to structure parameters of temperature, specific humidity, and the cross-correlation of temperature and specific humidity as seen in Equation (9).

$$C_n^2 = B_1 C_T^2 + B_2 C_{Tq} + B_3 C_q^2 \tag{9}$$

The parameters B_1, B_2, and B_3, are related to temperature, humidity, and pressure and are given in Fredrickson (2000) although minor corrections to the formulations are needed (Wauer 2018, personal communication). Equation (9) provides a method to calculate based on spatial variations in temperature (C_T^2) and humidity (C_q^2), as well as the correlation of temperature and humidity fluctuations C_{Tq} in Equations (6-8).

D. ATMOSPHERIC MODELS FOR OPTICAL TURBULENCE

The structure function parameter for index of refraction is not a direct measurement or forecast quantity, but it is a critical variable for quantifying the atmospheric effects on optical propagation. To obtain C_n^2 values for use in optical propagation models, there are various models using either modeled or observed meteorological data as input. The Navy Atmospheric Vertical Surface Layer Model (NAVSLaM) is a diagnostic model based on near surface mean quantities available from weather stations, or meteorological buoys, or atmospheric forecast models.

NAVSLaM is based on Monin–Obukhov Similarity (MOS) theory to derive mean vertical profiles of temperature and humidity within the atmospheric surface layer. Through this profile, it can generate the index of refraction profile for quantifying ducting conditions for radio frequency (RF) and microwave propagation. It is also capable of providing C_n^2 profiles within the surface layer based on the same local meteorological properties as those for RF propagation. “According to MOS theory, conditions are assumed to be horizontally homogeneous and stationary, and the turbulent fluxes of momentum, sensible heat, and latent heat are assumed to be constant with height in the surface layer” (Fredrickson, 2000). The key derived parameters in the MOS theory framework are the scaling parameters based on the kinematic turbulent momentum fluxes, sensible heat, and latent heat fluxes. The frictional velocity scale, the temperature and water vapor specific humidity scales are defined in Equations (10-12), where u is the

streamwise wind component, w is the vertical wind component and q is the specific humidity. The prime denotes turbulent perturbations.

$$u_* = < -w'u' >^{1/2} \tag{10}$$

$$T_* = \frac{- < w'T' >}{u_*} \tag{11}$$

$$q_* = -\frac{< w'q' >}{u_*} \tag{12}$$

These dynamic surface layer properties can form a non-dimensional parameter, ξ, shown in Equation (13), which is used to define the thermodynamic and turbulent characteristics of the surface layer. Based on MOS theory, all other scaled properties of the surface layer can be expressed as a function of ξ. Note in Equation (13), z is the height above the surface, g is acceleration due to gravity, θ_v is virtual potential temperature and k is the Von Kármán constant.

$$\xi = \frac{zkg(T_* + 0.61Tq_*)}{\theta_v u_*^2} \tag{13}$$

MOS theory gives the structure parameters for temperature, humidity, and their cross-correlation C_T^2, C_{Tq} and C_q^2, respectively in Equations (14-16):

$$C_T^2 = T_*^2 z^{-2/3} f_T(\xi) \tag{14}$$

$$C_{Tq} = r_{Tq} T_* q_* z^{-2/3} f_{Tq}(\xi) \tag{15}$$

$$C_q^2 = q_*^2 z^{-2/3} f_q(\xi) \tag{16}$$

Where f_T, f_{Tq} and f_q are empirically determined dimensionless functions and r_{Tq} is the temperature-specific humidity correlation coefficient. In the atmospheric surface layer, C_T^2, C_{Tq} and C_q^2 vary with height following $z^{-2/3}$. In the case of an unstable surface layer (when $\xi \le 0$), the form of f_T is given by Equation (17) (Edson & Fairall, 1998).

$$f_T(\xi) = f_q(\xi) = 5.9(1-8\xi)^{-2/3} \tag{17}$$

Monin–Obukhov similarity theory is limited to the homogeneous surface layer where flux is assumed to be constant with height. Previous studies showed good agreement between the MOS-derived C_n^2 and those from scintillation measurements in unstable conditions, while large discrepancies were found in stable conditions. MOS C_n^2 scintillation estimates are much higher than the scintillation values in stable conditions as the air-surface temperature difference increases. Unfortunately, MOS also breaks down as the separation from the surface increases above the surface layer as turbulent fluxes are not constant with height. Non-stationary and heterogeneous conditions are frequently observed in the atmosphere (Foken, 2006). Hence, one should be cautious in using the MOS theory-based C_n^2 profiles.

The Hufnagel-Valley Model is an optical turbulence model providing direct calculations of C_n^2 which assumes a low tropopause height and works best in the mid-latitudes. The model is based on wind speeds (W) and C_n^2 values at one meter above the ground. The Hufnagel-Valley model is useful because it can extend into the upper atmosphere beyond the boundary layer. This empirical model helps in scaling the atmosphere from surface-based measurements. However, because of its assumptions above the measurement source, it needs to be used with caution due to its inherent limitations. Equation (19) gives the formulation of the Hufnagal-Valley model, where h is the height above ground and A is the relative strength of the turbulence near the ground level (ex. 1.7 x 10^{-14} $m^{-2/3}$) (Lawson & Carrano, 2006).

$$C_n^2(h) = 5.94\times10^{-53}\left(\frac{W}{27}\right)^2 h^{10}e^{-h/1000} + 2.7\times10^{-16}e^{-h/1500} + Ae^{-h/100} \tag{18}$$

In order the predict how well the laser beam maintains its energy focus while propagating through the atmosphere, the C_n^2 values need to be accurately specified. Increased observational data collected at high sampling rates will help to validate and/or improve C_n^2 models. The Laser Environmental Effects Definition and Reference (LEEDR) model is another environmental model, also sponsored by the DoD's Directed

Energy Joint Technology Office, to characterize C_n^2. To properly model the lower atmosphere, LEEDR creates vertical profiles of meteorological data including effects from gas constituents, aerosols and optical turbulence. (Center for Directed Energy, 2018)

E. HIGH ENERGY LASER SYSTEM PERFORMANCE MODELS

System performance models use C_n^2 values as input to demonstrate how a HEL system will perform under the given atmospheric environment. One system performance model is the High Energy Laser End-to-End Operational Simulation (HELEEOS), sponsored by the DoD's Directed Energy Joint Technology Office. HELEEOS is a software tool used to help design directed energy weapons which accounts for atmospheric and beam propagation effects. (Center for Directed Energy, 2018)

Another system performance model is the High Energy Laser Code for Atmospheric Propagation (HELCAP) developed by the Naval Research Laboratory. The program allows the input of lasers of energy levels ranging from megawatt to terawatt to be modeled in a 3-D propagation simulation. HELCAP also takes inputs from the environment to predict loses and is especially tuned for the maritime environment (NRL 2018).

F. OTHER FACTORS AFFECTING HEL PROPAGATIONS

Absorption and scattering effects are derived from the composition of molecules and aerosol particulates in the atmosphere. Absorption occurs when particles collect the energy of the electromagnetic (EM) waves passing into their EM field. The absorption of the energy temporarily raises the energy state of the particle's electrons before they are emitted at a lower frequency. Scattering occurs when particles absorb and immediately release the energy, but the direction of the outgoing radiation changes from its incident direction.

Aerosols within the atmosphere can be broken down into both hygroscopic and non-hygroscopic categories. Hygroscopic aerosols typically absorb energy within the HEL wavelengths which can lead to their vaporization. Whereas, non-hygroscopic

aerosols (dust, soot), which have large scattering and absorption coefficients, will not vaporize and will instead heat the surrounding air, which produces secondary propagation effects.

Two other transmission effects which can modify HEL propagation are beam spread and beam wander. Beam spread is caused by laser defects which affect beam quality. Beam spread causes the light to broaden and lose its focus at the target. Beam wander is caused by variations in the index of refraction due to turbulence (at a larger scale than scintillation) which causes the beam to tilt and deflect from its intended target. (Sprangle 2005).

G. SUAS-BASED MEASUREMENTS FOR QUANTIFYING THE LOWER ATMOSPHERE

A sUAS can be an ideal platform for quantifying the atmospheric properties affecting laser propagation along the path. Taking spatial meteorological measurements in the lower atmosphere can be difficult using traditional measurement platforms, such as manned aircraft, land towers, or surface buoys. It can be especially hazardous for manned fixed wing aircraft to fly within a 100 m of the surface (as well as costly) for the most precise measurements affecting HEL propagation. Towers unfortunately can only sample at a single point at a fixed height and are unable to survey the large volumes necessary for accurate statistics within the surface layer.

Fortunately, sUASs have a niche within this region of the atmosphere. They can fly at relatively low speeds (10-15 ms^{-1}), at levels from just above the ground to the top of the boundary layer (10-300 m) and they can survey a significant air parcel ($\geq$1 km^2) over the course of an hour of flying. Additionally, they can fly a given pattern with very little human input, which makes beyond visual line of sight possible.

C_n^2 values within the boundary layer can change rapidly with height and horizontal distance due to local temperature gradients and surface morphology. The low flight speed enables the sensors to resolve the small temperature perturbations. Also, the ability to cover a large swath of the atmosphere in short order is critical to observing these time-sensitive effects throughout the air column before they evolve with the day.

These factors make them well suited to measuring turbulence effects for HEL propagation. The characteristics of various UAVs for atmospheric applications are shown in Table 1. Each platform comes with its own benefits and drawbacks.

Table 1. Characteristics of some sUAS currently used for meteorological measurements. Source: Dias et al. (2012).

UAV	Wing Sp (m)	Payload (kg)	Endurance	Cruise speed ($m s^{-1}$)	Height (m a.g.l.)
RPMSS	3.00	4 (est.)	4–8 h	18–20	5,000
Aerosonde	2.90	5	40 h	20–32	6,000
BAE Manta	2.70	5.4	5 h	21	3,500
M2AV	2.00	1	<60 min	20	800
Powersonde	~1	1	~1 h	13	6,000
Smartsonde	1.74	1 (est.)	15 min	15	>300
SUMO	0.80	0.2 (est.)	20 min	12–18	3,500
Aerolemma-3	1.20	1.2	15 min	17	2,000

H. METEOROLOGICAL SUAS

Shipboard and ground-based meteorological observations are commonly taken for situational awareness. Unfortunately, in situ measurements above the surface within the lower atmosphere throughout the DoD operational environment are rare. Unfortunately, artillery MET teams and surface-based upper air soundings only give a coarse resolution of the boundary layer. Fortunately, an sUAS can fill this gap between surface-based measurements and manned aircraft measurements. Additionally, this capability can be compounded with multi-sUAS cooperative flights for denser sampling or an increased target volume.

Lighter and lower power sensors are enhancing the abilities of a sUAS to host an array of sensors that would typically require the payload capacity of a manned aircraft. An array of various meteorological sensors can be found below in Table 2.

Table 2. sUAS sensors for various meteorological variables.
Source: Elston et al. (2015).

UA	Wind	Humidity	Temperature	Pressure
Cruiser	GP/IMU/ dynamic pressure	Varies	Varies	Varies
UMARS 2	Five-hole hemisphere	Thermocouple	Meteolabor AG "Snow White" dewpoint hygrometer	Measured around five-hole hemisphere
Manta	Nine-hole probe	Vaisala HMP45C	Vaisala HMP45C	All sensors barometric sensor
ScanEagle	Nine-hole probe	Vaisala HMP45C	Vaisala HMP45C	All sensors barometric sensor
Aerosonde	Proprietary algorithm	Vaisala RS90	Vaisala RS90	Vaisala RS90
RPMSS	GPS/INS	Humidity sensitive capacitor	Thermal resistor	MEMS
Tempest	Aeroprobe five-hole probe	Vaisala RS92	Vaisala RS92	Proprietary autopilot sensor
M^2AV	Five-hole probe	Vaisala HMP50	Vaisala HMP50 and thermocouple	Sensortechnics 144SC0811Baro
CU NexSTAR	Proprietary algorithm	Vaisala RS92	Vaisala RS92	Proprietary autopilot sensor
MASC	Five-hole probe	Custom (Wildmann et al. 2013)	Thin wire and thermocouple (Wildmann et al. 2013)	Sensortechnics 144SC0811Baro
Aerolemma-3	None	CSI HMP50	CSI HMP50	CSI CS100
SMARTSonde	GPS/infrared	Sensiron SHT75	Sensiron SHT75/VTI SCP1000	VTI SCP1000
Powersonde	None	NSSL Radiosonde	NSSL Radiosonde	NSSL Radiosonde
Kali	None	Honeywell HIH-3605-B	National Semiconductor LM50 C	Motorola MPX 2100
DataHawk	GPS/infrared	Honeywell capacitive polymer	TI ADS1118	MS5611–01BA03
SUMO	GPS/IMU	Sensiron SHT75	Sensiron SHT75 / PT1000	VTI SCP1000

THIS PAGE INTENTIONALLY LEFT BLANK

III. METHODS

A. AIRFRAME

The Penguin airframe (Figure 5) was selected to host our airborne sensor suite. It is adapted from the Finwing Penguin built for the first-person-viewpoint (FPV) hobby market. The airframe includes a raised pusher propeller setup that places the propulsion downstream of the meteorological sensors which are located at the nose of the fuselage. The aircraft is predominantly made from durable EPP foam. It includes oversized control surfaces giving it excellent control authority for stable flight. It includes a large payload bay that provides sufficient internal volume for any conceivable sensor payload. It also has an extended battery tray allowing for oversized batteries to increase endurance. This extended tray also allows for repositioning of the battery to adjust the center of gravity to accommodate various sensor payloads. The instrumented Penguin was initially tested for meteorological measurements during Joint Interagency Field Experimentation (JIFX) 15–3 in 2015 with satisfying flight characteristics.

Figure 5. NPS Penguin flying over Camp Roberts on 13 May 2015

The Penguin flies at an air speed of 13 to 40 knots and an ascend/descend speed of up to 7.5 m/s. Baseline tests in earlier flights show that cruise flights of 80-minute duration are possible, however, given the demanding flight profiles used for meteorological soundings, typical test flights ranged between 30–40 minutes depending

on altitude gain. The aircraft's dimensions are 123 cm long with a wingspan of 172 cm with a 25 cm propeller behind the instruments bay.

The Penguin was controlled through a wireless connection to a laptop ground control station shown in Figure 6. The Mission Planner software was linked to the Pixhawk autopilot onboard the Penguin. The Pixhawk autopilot can take over complete flight control of the Penguin when initiated by the manual operator. The ground control station allowed for beyond visual line of sight (VLOS) flights, however, we flew within line of sight (LOS). Even with this restriction, the Penguin can quickly and accurately cover an extended region of the lower atmosphere. The onboard autopilot setup makes it possible for a ground control system (GCS) operator to fly the aircraft on pre-programmed tracks remotely from the ground at a constant heading and altitude despite variable winds aloft.

Figure 6. Ground control station for Penguin

To fly the Penguin at Camp Roberts, the sUAS needed to have a suite of failsafe actions programmed into the autopilot. First, a geofence was setup which contained the Penguin within a specified box while in flight. If the Penguin passed through the geofence's floor or ceiling altitudes, or it exited the boundary which encircled the runway, it would be re-directed to a rally point over the runway. Additionally, if the

Penguin's battery voltage or remaining power dropped below a minimum threshold, it would also return to the rally point. Finally, if communication was lost between the Penguin and the ground control station, the Penguin would cycle back to the set rally point. A screenshot of the Mission Planner GUI for generating autonomous flights is shown in Figure 7. The thick pink line denotes the geofence box, the yellow line the sUAS's intended track, and the red pin indicates the rally point. The purple line indicates the actual path flown in recent history, and the red line indicates the current heading of the aircraft. The offset of the heading and the flight path indicates that the aircraft is crabbing to compensate for a significant cross wind.

Figure 7. Mission Planner GUI for generating autopilot flights

B. SENSOR INTEGRATION

The sensor payload development for the NPS Penguin aimed at characterizing the meteorological conditions of the atmospheric boundary layer affecting optical wave propagations. The necessary complete dataset comes from several components: sensors integrated in the Penguin's autopilot system, a radiosonde sensor package, and a high-rate temperature sensing unit. The Penguin's Pixhawk autopilot system is integrated with a pitot tube, a GPS receiver, and a barometer. It logs flight attitude angles, air speed,

altitude, pressure, and GPS locations. The autopilot altitude is a blend of GPS altitude and pressure altitude derived from the barometer pressure. Wind direction and speed were derived through onboard calculations within the Pixhawk and were logged as output. All temperature sensors are all mounted outside the skin of the Penguin to measure the undisturbed air outside of the fuselage (Figure 8).

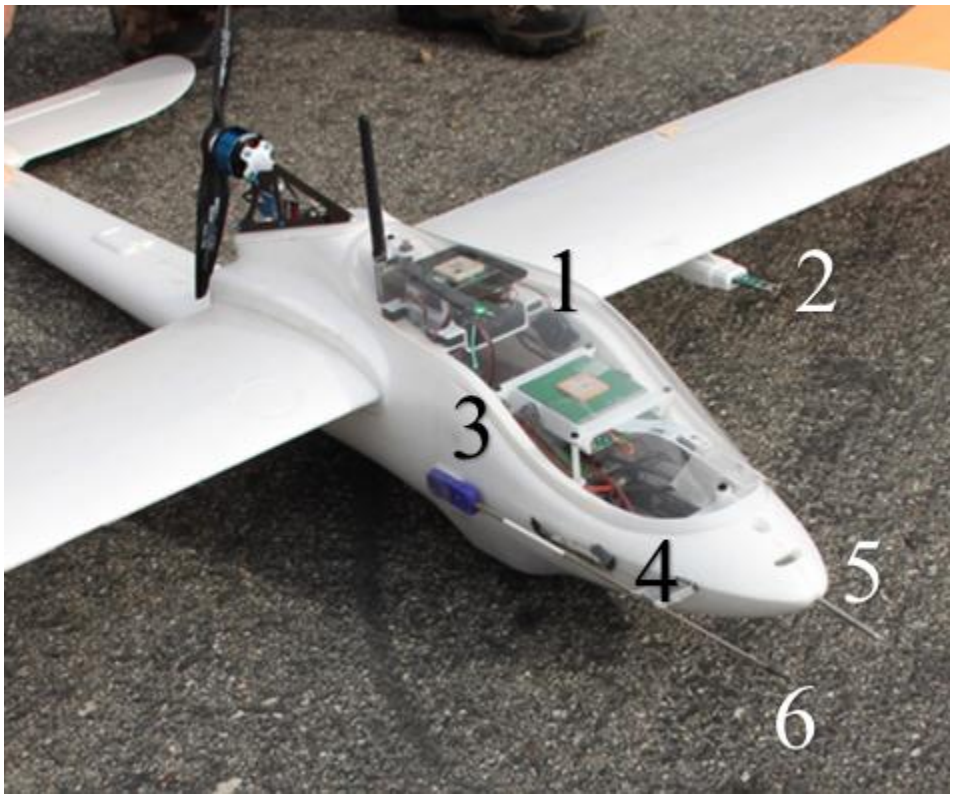

1) Pixhawk Autopilot 2) iMet-XQ 3) iMet Radiosonde, 4) Resistance Temperature Detector (RTD) Platinum Temperature Sensor and 5) Pitot tube 6) Thermocouple

Figure 8. Illustration of the Penguin's sensor housing bay

There are two iMet sounding systems installed onto the Penguin to measure the mean temperature, humidity, and pressure. One is the multi-parameter weather sensor (iMet-XQ) under the port wing, the other is the non-transmitting iMet-1 radiosonde hosted within the sensor bay with the sensor head outside in the free air stream. Both systems also record GPS coordinates, although at a lower sampling rate (1 Hz) compared to that within the Penguin's avionic system (10 Hz).

The temperature sensing package directly supporting optical turbulence characterization includes a platinum temperature sensor and a thermocouple. The platinum temperature sensor is a high accuracy, slow response probe to measure mean temperature. The 0.001 in diameter fine-wire thermocouple measures atmospheric temperature gradients or fluctuations with research-grade accuracy. The small diameter of the fine wire thermocouple results in a negligible amount of solar heating and hence removes the need for a solar radiation shield. The small diameter also allows for fast response of the sensor to ambient temperature perturbations, resulting in fast temperature measurements suitable for C_n^2 calculation or flux calculation using the direct eddy correlation method. A reference temperature is needed for the thermocouple data reduction. The RTD probe described earlier covers this gap. The instruments onboard the Penguin are characterized in Table 3. An image of the fine-wire thermocouple is shown in Figure 9.

Table 3. Instruments onboard the Penguin

Instrument	Range	Accuracy	Precision	Sampling Rate (Hz)
Pixhawk GPS (#1) [m,deg]	----	1	0.0001	10
InterMet XQ Multi-parameter weather sensor (#2)				
Temperature [°C]	-95-50	±0.3	0.01	1
Humidity [%RH]	0-100	±5	0.1	1
Pressure [hPA]	10-1200	±1.5	0.1	1
iMet-1 Radiosonde unit (#3)				
Temperature [°C]	-95-50	±0.2	0.01	1
Humidity [%RH]	0-100	±5	0.01	1
Pressure [hPA]	10-1200	±0.5	0.01	1
Fluke Pt100 RTD (.02") Platinum temperature sensor (#4) [°C]	-200-350	±0.15 at 0 °C	0.001	2.5
Pixhawk PX4 Static Pitot Tube (#5) [% hPA, hPA]	-170-250	±0.25	0.0001	2
Campbell Scientific Fine Wire (.001") Thermocouple sensor (#6) [°C]	-95-50	±1	0.001	10

Figure 9. Picture of the thermocouple used on NPS Penguin. Source: Campbell Scientific (2018).

Data acquisition on the Penguin is done by several different systems. The two iMet radiosonde systems and the Penguin's autopilot system each record their own data. The thermocouple and the RTD temperature are logged through a Teensy 3.x, which is a

lightweight (0.153 oz.) and low power consumption microcontroller that can perform analog-to-digital sampling of multiple data streams and stores the data on a microSD card for post-processing. To merge the data from different subsets into one coherent dataset, GPS time was used as the common variable. However, some fine tuning was required using the correlation coefficients of variables simultaneously logged on different systems.

C. GROUND TESTING

Ground testing is designed to cross-check the capability of the Penguin sensor suite in sampling and logging high-rate temperature. A side-by-side comparison was conducted over an airport taxiway. This compared the Penguin temperature measurements against measurements using a Campbell Scientific InfraRed Gas Analyzer SONic anemometer (IRGASON) on a standard data logger such as the Campbell Scientific CR6. The test was conducted at the Marina Municipal Airport, which hosts the NPS Center for Interdisciplinary Remotely-Piloted Aircraft Studies (CIRPAS). The test area is shown in Figure 10 where the ~500 m section of the tarmac is outlined by the yellow loop.

Figure 10. Path of track for sensor evaluation at the CIRPAS runway. Adapted from Google Earth 2018.

During the sensor testing, only the thermocouple and the RTD sensors were mounted on the Penguin as described earlier. The Penguin's fuselage was mounted next to an IRGASON sonic anemometer and gas analyzer integrated with a separate thermocouple shown in Figure 11. The two-thermocouple setup was specifically designed to allow an evaluation of the data acquisition of the Penguin's Teensy to the Campbell Scientific CR6.

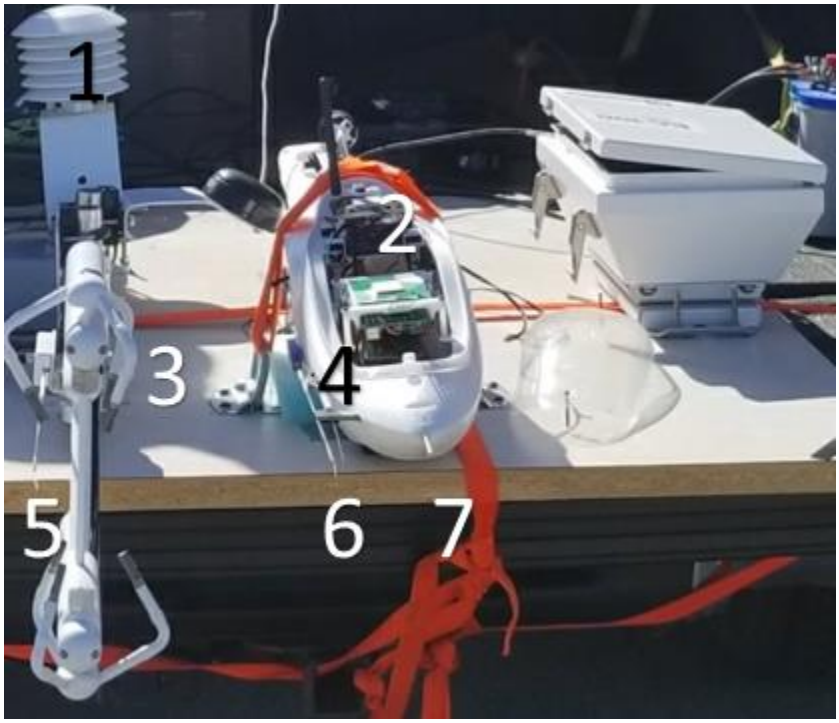

1) Sonic Anemometer Temperature Sensor, 2) Pixhawk Autopilot, 3) Sonic Anemometer, 4) RTD Platinum Temperature Sensor, 5) Thermocouple logged by CR6 6) Thermocouple logged by Teensy and 7) Pitot Tube

Figure 11. Tailgate setup during Marina testing

The platform containing both the Penguin's fuselage and the sonic anemometer were mounted on the rear tailgate of a Ford F-150 pickup truck. To reduce airflow effects from the vehicle, the platform was then driven in reverse at various ground speeds ranging from 2 ms^{-1} to 12 ms^{-1} (the approximate flight speed of the Penguin is 12 ms^{-1}). Complete loops were driven both north and south at increments of approximately 1 ms^{-1}.

D. FLIGHT TESTING

Flight testing was conducted at the McMillan Airfield, which is located at the California Army National Guard Camp Roberts base in California. McMillian Airfield (Figure 12) provides Naval Postgraduate School with a safe location for UAV operations inside of restricted airspace R2504. The airfield is isolated and hosts clear airspace with limited signal interference. Additionally, given its location 25 miles east of the Pacific Ocean in Central California, it manages approximately 250 flyable days a year (Pike, 2018). The runway is 3500’ long, 65’ wide with 10’ shoulders at a heading of 281 degrees.

Figure 12. Area of Operations at McMillan Air Field, Camp Roberts. Adapted from Google Earth (2018).

The focus of the Penguin flights at the McMillian Airfield was to determine the feasibility of quantifying optical turbulence using sUAS based payload systems. For accurate turbulence statistics, it is desirable to fly sections of straight and level legs at constant heading and altitude. A dog bone pattern is normally used as shown in Figure 13 overlayed on a GoogleEarth view of the McMillian airfield. Figure 14 shows the flight

trajectory from Flight 5 taken on 26 March 2018. The rounded ends of the dog bone pattern allowed for altitude gain/loss separate from the straight and level sections to ensure consistency of direction and altitude. For each flight, level legs were spaced out between 5-25 m. The altitude separation between passes was small at low altitudes in order to resolve the strong vertical gradient in the mean and turbulence variables. The inter-level altitude separation was increased for altitudes above ~100 m. An example of the flight altitude and its variation along the runway is shown in Figure 15 during the March 2018 testing. Within about 30 minutes of flight time, 15 to 24 flight legs were flown between ~15 m and 300 m above the ground. The flights were flown at a mean airspeed of approximately 12 ms^{-1}. Launch and landing flight segments were performed by a remote control (RC) pilot, although subsequently, autonomous hand-launch and autonomous landing capabilities have been developed, minimizing the requirement for a RC pilot. The picture of the Penguin as it approached the runway for landing is shown in Figure 16.

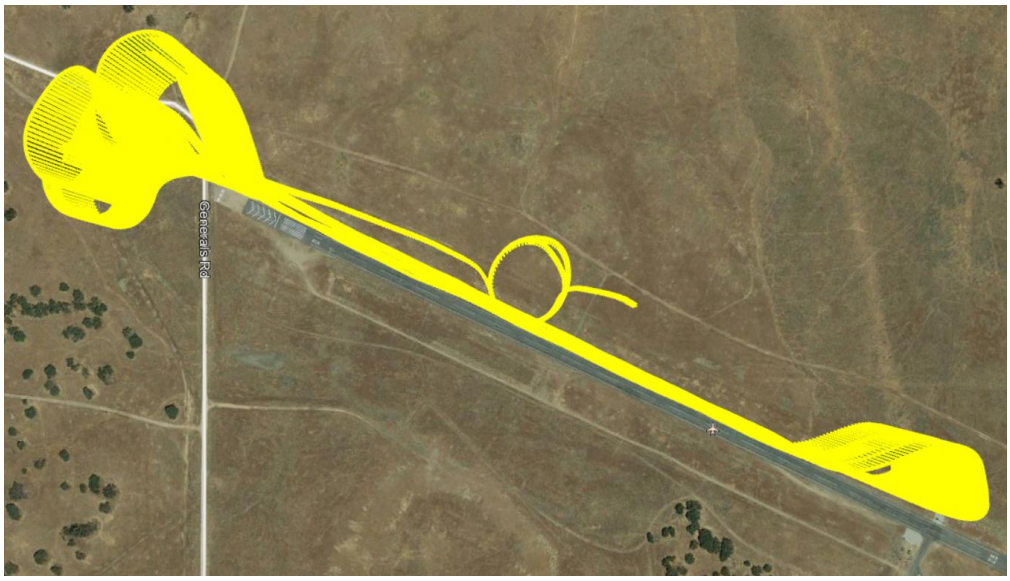

Figure 13. Dog bone flight pattern made by the NPS Penguin at McMillan airfield. Adapted from Google Earth (2018).

In addition to the level legs, one or two sounding legs were usually flown during each flight. The sounding profiles were conducted between 50 and 300 m. The purpose of

the ascent/descent soundings was to sample the vertical variations of the atmospheric properties within a short time period. The sounding legs typically consumed a majority of the battery's energy as they climbed at full throttle to reach peak altitude within the span of a single leg.

On 16 November 2017, the Penguin was used for a series of five flights over McMillian airfield. The weather was partly cloudy to cloudy with a moderate breeze strong enough to force a significant crab angle on the Penguin. The first flight was to test the fail-safes required for safe flight. The second and third flights included only straight and level legs. The fourth flight included both level legs as well as two soundings. The fifth and final flight included two soundings, and no level profiles.

On 26 March 2018, the Penguin was used for another series of five flights over McMillian airfield. The weather was sunny with light winds. On each flight, the penguin flew level legs at various altitudes with a single sounding.

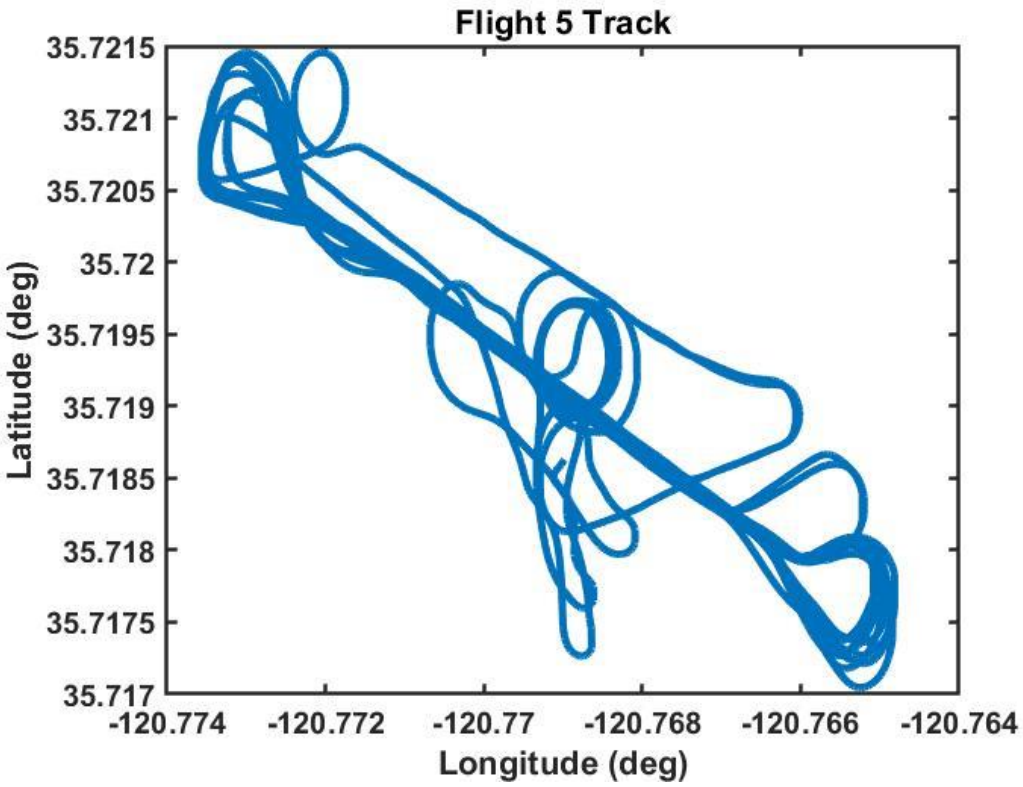

Figure 14. GPS Latitude and Longitude of Flight 5 taken on 26 March 2018.

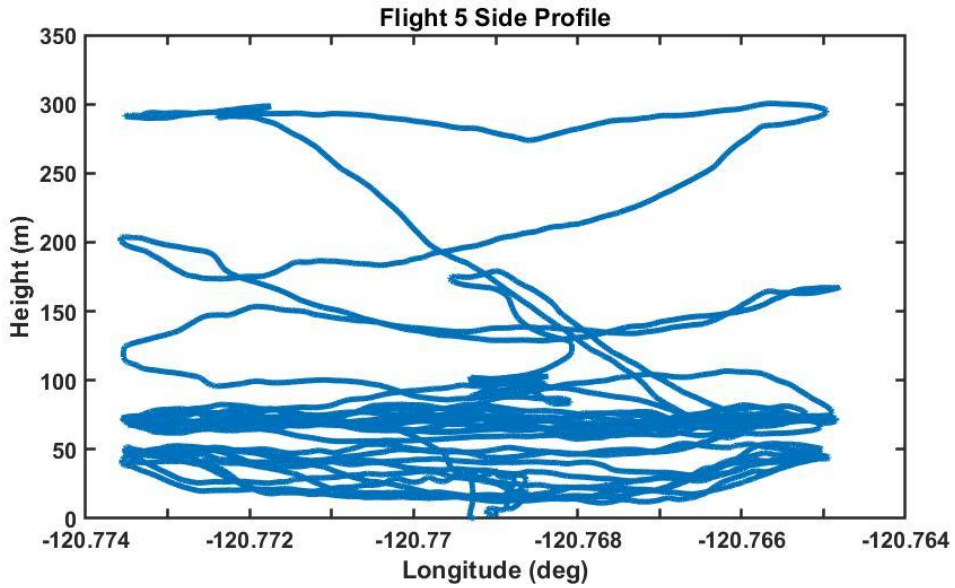

Results shown are from Flight 5 on 26 March 2018.

Figure 15. Flight altitude along the runway as indicated by longitude variations.

Figure 16. The NPS Penguin coming in for landing on one of the flights at McMillian airfield.

During the third flight on 26 March 2018, The Penguin landed into grass growing through the runway and unfortunately broke the thermocouple's fine wires. The problem was noticed at the end of the fourth flight and a new thermocouple was connected prior to the fifth flight. Hence, only data from four flights will be shown in the later discussions.

During this second series of test flights at the McMillian airfield, a tripod tower was setup next to the runway with an array of instruments to sample near-surface mean and turbulence as well as ground properties (Figure 17). The IRGASON sonic anemometer and H_2O/CO_2 gas analyzer on the tripod was setup at 2.57 m above the ground. Three sets of Campbell Scientific temperature/humidity sensors were set at 0.83, 1.69, and 2.77 m above the ground for sampling the mean gradient of temperature and humidity at levels closest to the surface. Surface soil temperature and moisture were also measured as part of the tripod sensor suite. The tripod-based measurements started before the first Penguin flight and ended after the side-by-side comparison measurements after the fifth flights. The mean meteorological conditions, turbulent flux transport, and C_n^2 can be obtained from the tripod-based measurements and can be used as a baseline to compare with the measurements taken by the Penguin. Figure 18 shows the tripod setup next to the runway during a Penguin flight.

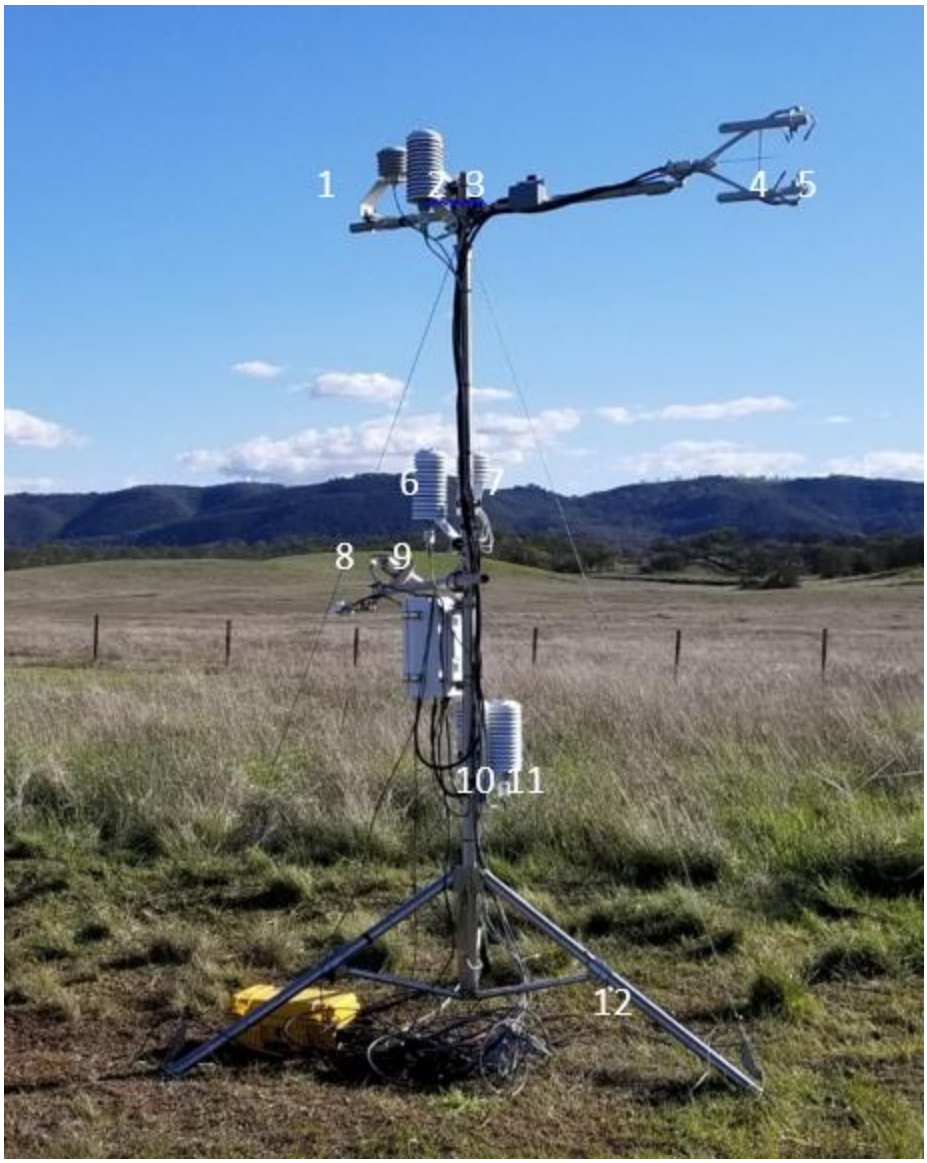

1) Sonic Anemometer Temperature Sensor, 2) Temperature Sensor, 3) Humidity Sensor, 4) Thermocouple logged by CR6 5) Sonic Anemometer, 6) Temperature Sensor, 7) Humidity Sensor, 8) Radiation detector, 9) IR Ground Temperature Sensor, 10) Temperature Sensor, 11) Humidity Sensor, 12) Ground Temperature Probe

Figure 17. Sensor package on the tripod tower. Sensors corresponding to each number are given in Table 4.

Table 4. Sensors on the tripod tower for near surface air and soil properties measurements

Instrument	Range	Accuracy	Precision	Sampling Rate (Hz)	Height (m)
Vaisala HMP155 Temperature sensor (#3, 7, 10) [°C]	-20 - 60	±(0.07+0.25%)	0.001	1/5	2.77, 1.69, 0.83
Vaisala HMP155 Relative Humidity (#2, 6, 11) [%RH]	0 - 100	±1.0	0.01	1/5	2.77, 1.69, 0.83
Campbell Scientific IRGASON (#5) Infrared Gas Analyzer [g/m^3]	0 - 42	±(0.037 + 0.3%)	0.0035	50	2.57
Campbell Scientific IRGASON (#5) 3-D Sonic Anemometer [m/s]	-65 - 65	<±0.08	0.001	50	2.57
Campbell Scientific IRGASON Temperature CS109 (#1) [°C]	-30 - 50	±0.15	0.001	50	2.57
Campbell Scientific Fine Wire Thermocouple sensor (.001") (#4) [°C]	-30 - 50	±2.0	0.06	50	2.57
Heitronics CT15 Series Infrared Thermometer (#9) [°C]	-90 - 150	0.7% ± 0.8	0.01	1	1.56
Campbell Scientific Ground temperature SS109 (#12) [°C]	-30 - 50	±0.15	0.001	50	0
Kipp-Zonen CNR4 Net Radiometer Infrared Up/Down-Welling (#8) [W/m^2]	0 - 2000	<5% (~1σ)	0.005	1	1.44
Kipp-Zonen CNR4 Net Radiometer Solar (#8) [W/m^2]	0 - 250	<10% (~1σ)	0.007	1	1.44

Figure 18. Tripod, Penguin and Ground Control Station

A side-by-side comparison measurement was made at the end of the fifth and final flight when the Penguin (without the wings) was attached to a second tripod at the same level above the ground as the sonic anemometer on the instrumented tripod tower (Figure 19). The simultaneous data collection on both systems lasted for approximately 30 minutes.

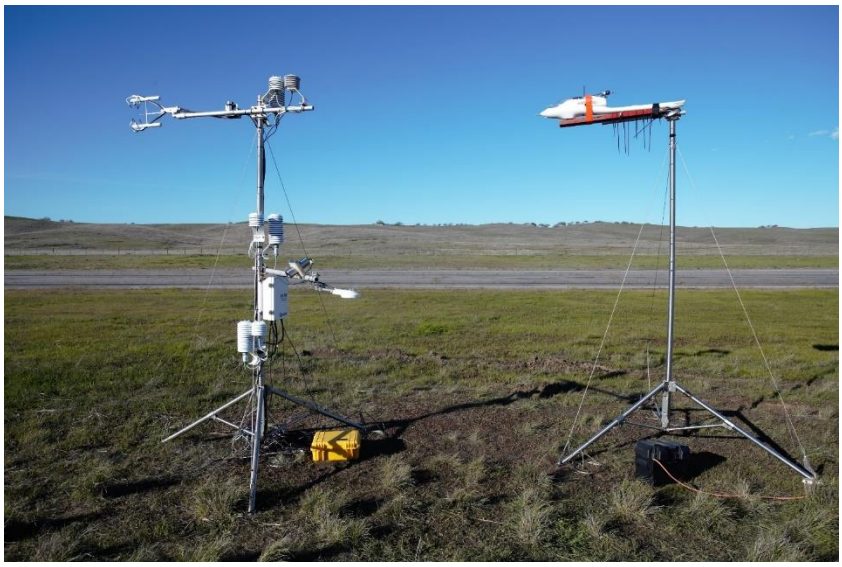

Figure 19. Side-by-side sensor data collection test

A meteorological tower was setup and maintained by the NPS Meteorology Department close to the McMillian airfield runway (Figure 20). The tower measures air pressure, temperature, dew point, wind speed and wind direction measurements. This data was also used to illustrate the general meteorological conditions during the test days.

Figure 20. McMillian meteorology sampling tower

IV. RESULTS

A. RUNWAY TESTING RESULTS

The ground testing on the runway of Marina Airport was intended to test two aspects of the sUAS sensor payload. First, it was to test the adequacy of the fast response thermocouple in comparison with the temperature measurements from the 3-D sonic anemometer in detecting turbulence generated temperature perturbations. Second, it was to test the thermocouple measurement logging adequacy of the Teensy installed on the Penguin. It is important that the thermocouple temperature perturbations are sampled adequately to resolve the small eddies in the turbulent inertial subrange.

As described in Chapter III, two temperature measurements were made by the sUAS payload by a thermocouple and a RTD thermometer. Another two sets of temperature measurements were made from the IRGASON setup on the truck bed including those from the thermocouple installed close to the IRGASON's sonic path and by the sonic temperature. Figure 21 shows a 15 second data section to illustrate the comparison of the four temperature measurements. We find that all sensors, except the RTD one, gave similar results. Multiple hot plumes of air are indicated in Figure 21 and the data is highly skewed to the positive anomalies, suggesting the presence of strong warm plumes in the daytime surface layer. In particular, the temperature perturbations read by the Penguin's thermocouple align well with those of the thermocouple mounted on the IRGASON. Since the same type of sensors were used, the similarity between the two measurements, taken side-by-side on the bench of the truck, suggests the effectiveness of the Teensy micro data logger compared to the traditional Campbell Scientific CR6 datalogger normally used for fast-response sensors. Figure 21 also shows that the sonic temperature from the IRGASON in general had warmer plumes, especially in the warmest parcels, compared to both thermocouples. It is understood that the sonic temperature is very close to virtual temperature (de Szeoko et al. 2017). The warmer sonic temperature is likely a result of the water vapor contribution.

Figure 21 reveals the need to correct the drift in the thermocouple or the sonic temperature when compared to the slow but accurate RTD thermometer. However, this may not be a serious problem for our specific application of determining the structure function parameter since we are concerned with small turbulent eddies in the inertial subrange.

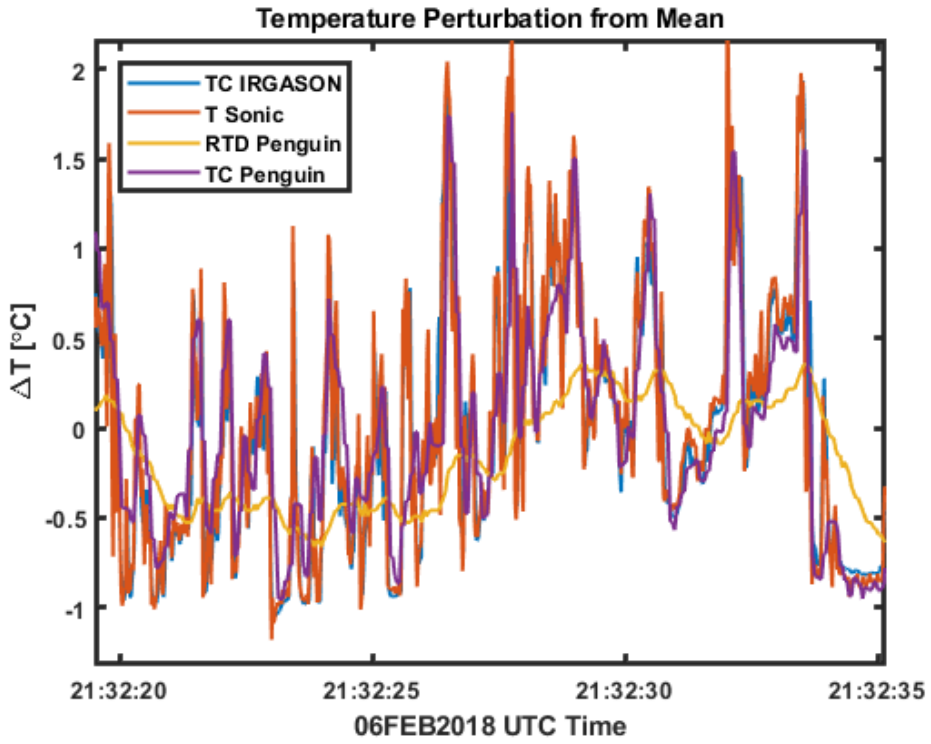

Slow response platinum temperature sensor (RTD Penguin), the thermocouple on the Penguin (TC Penguin), the thermocouple on IRGASON (TC IRGASON), and the IRGASON sonic anemometer (T Sonic).

Figure 21. Temperature perturbations from the four ground testing thermometers.

Spectral analyses were performed on various temperature measurements shown in Figure 21 and the results are given in Figure 22. Here, we particularly compare the representation of the spectra in the inertial subrange and how they compare to the theoretical -5/3 law (thick black lines). The thermocouple attached to the sonic anemometer lines up almost directly to that of the sonic anemometer, both logged with the Campbell Scientific CR6. All three fast thermometers seem to show that the

frequency band in the inertial subrange followed the -5/3 law. There is a slight dip in the energy density around 3 Hz to 5 Hz from the thermocouple on the Penguin. Additionally, since the Penguin is sampling at 20 Hz instead of 50 Hz, as with the CR6 datalogger, the thermocouple on the Penguin only resolves up to 10 Hz. Hence, the Teensy seems to sample for frequencies below 3 Hz, even though it resolves the eddies up to 10 Hz.

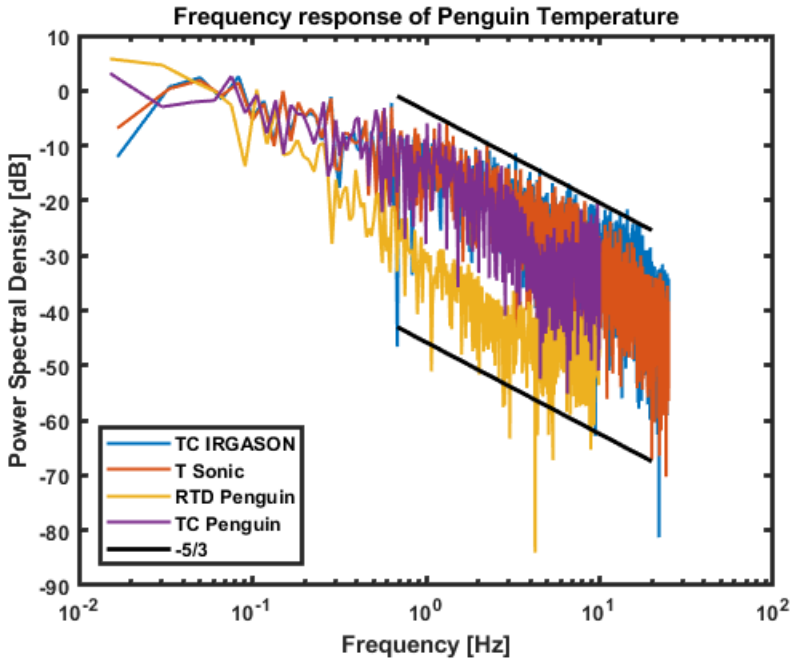

The solid black lines represent a spectrum with a -5/3 frequency relationship.

Figure 22. Energy density spectrum of all temperature sensors during the runway testing.

B. PENGUIN FLIGHT CHARACTERISTICS AND DATA QC

The Penguin made a series of dog bone pattern legs at various altitudes during its data sampling flights as shown in Figures 14 and 15 in Chapter III. Such a flight pattern was the most time/power efficient in generating straight and level legs from which turbulence statistics could be derived. An example flight pattern is shown in Figure 23 for Flight 2 on 26 March, 2018 overlaid with the track of all level legs (colored lines). The various paths which fall outside of this track are from take-off, landing and the offset sounding profile where the aircraft climbed to its maximum height.

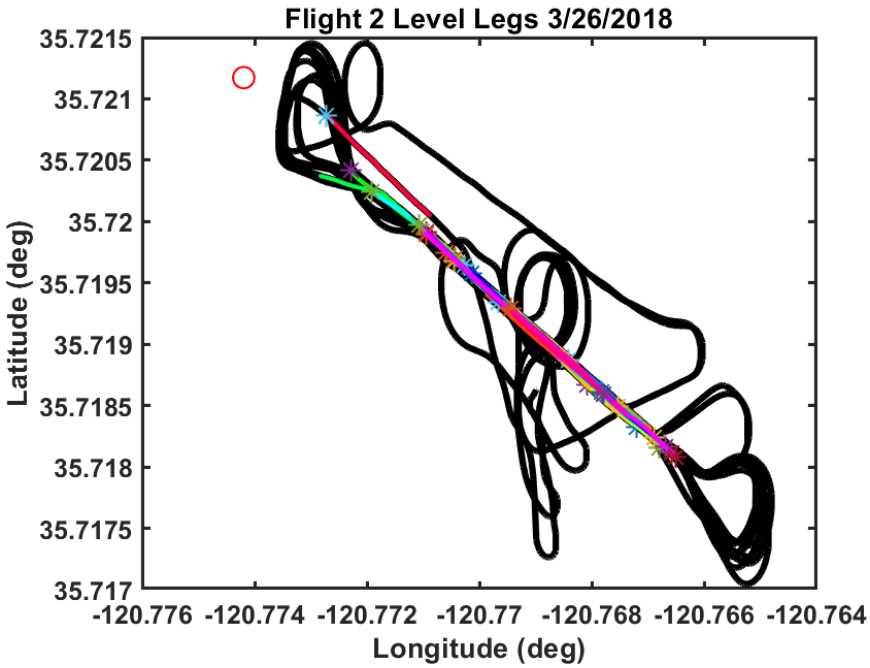

Each of the level leg cuts are displayed in the colored sections. The orange circle is a reference point from which distance along the track of all level legs were calculated. The '*' denotes the beginning of each leg.

Figure 23. Flight track of Flight 2 on 26 March 2018.

To generate accurate C_T^2 profiles from the Penguin, straight legs with little altitude variation were also preferred. An example of the fight altitude and its variation is shown Figure 24. To modify the altitudes from mean sea level (MSL) to above ground level (AGL), a difference of between 269 m-274 m was added to the original altitude values based on its ground value before flight. Note the large spike in altitude in the middle of the flight is from its sounding profile as it climbed up to 300 m. The significant altitude variations near the end of its flight are due to the low-level legs which came within under 15 m of the surface. In order to fly level legs at these levels, while ensuring sUAS safety of flight, the dog bone end turns were made at ~40-50 m before dropping down 10-25 m.

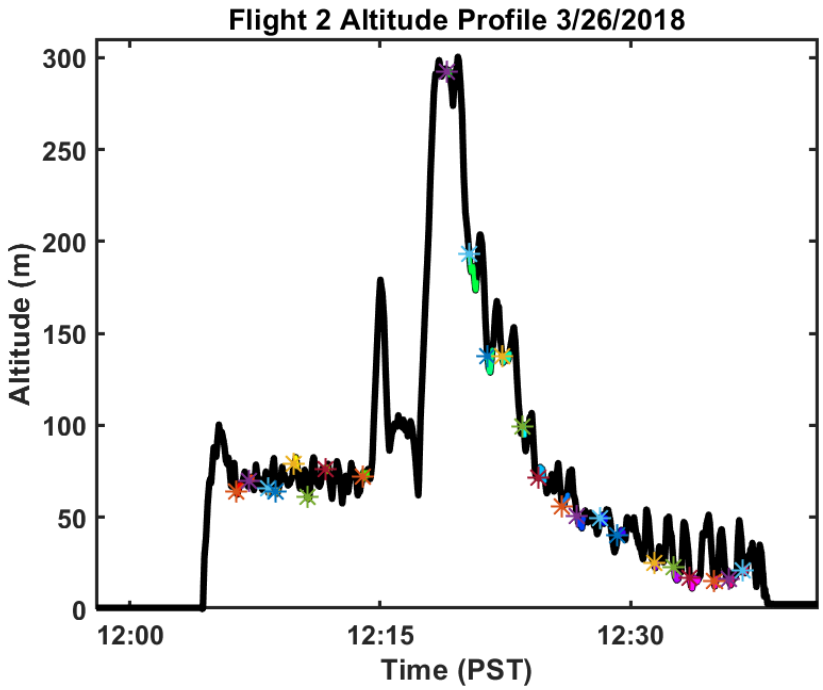

Data were taken during Flight 5 on 26 March 2018. Colored sections denote the time periods of level flights where the "*" denotes the beginning of each leg.

Figure 24. Flight altitude variation during a single flight.

The time sections of the straight level legs were selected manually. In selecting the start and end of each level leg, we plotted the temporal variations of altitude and heading to create precision cuts for the best accuracy. Figure 25 gives a snapshot of this process. Only small altitude variations were permissible for accurate statistics.

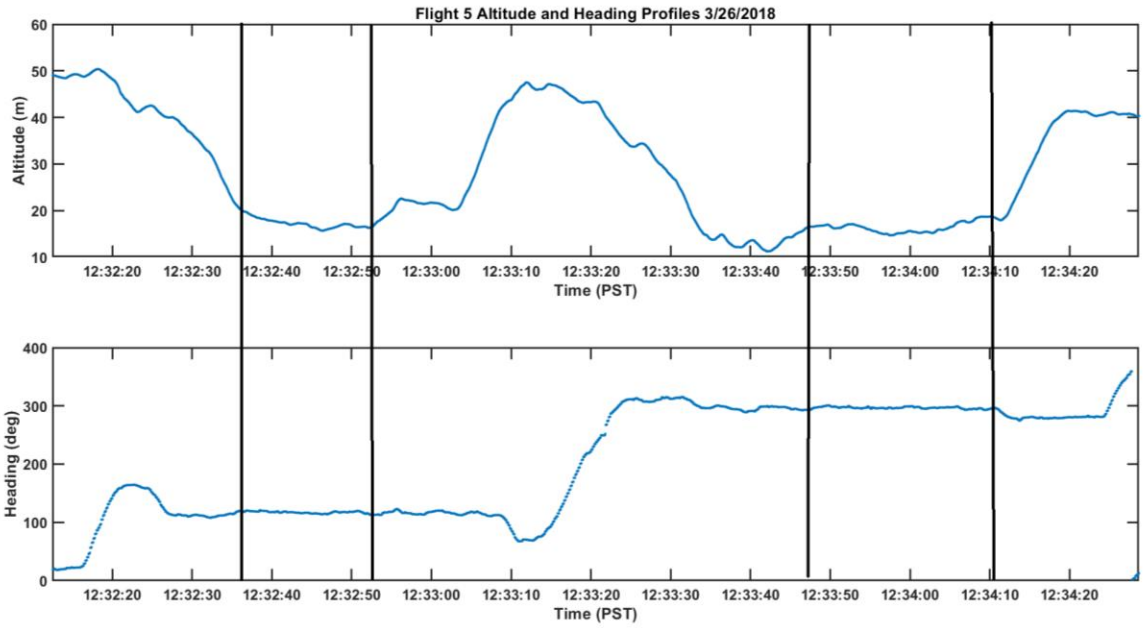

This side-by-side illustrates data splitting for mean turbulence statistics. In this example, the section between each of the two vertical black lines is considered a 'good' section with straight level flight.

Figure 25. A snapshot of the Penguin's altitude and heading over time.

The permissible altitude variations were kept small, usually within several meters at most, especially close to the ground compared to legs at higher levels. This adjustment is needed because of the strong gradients of the mean and turbulence variables near the surface. Hence, deviations in altitude may result in vertical variations being aliased into the perceived horizontal variations. Larger variations in altitude were allowed in the upper levels of the surface layer, given that the vertical variation of the turbulence quantities are relatively small. The altitude variations of the four flights flown on 26 March 2018 are shown Figure 26 where the standard variations of altitude from each selected level leg are shown as the length of the error bars extending up and down from the mean altitude of the leg.

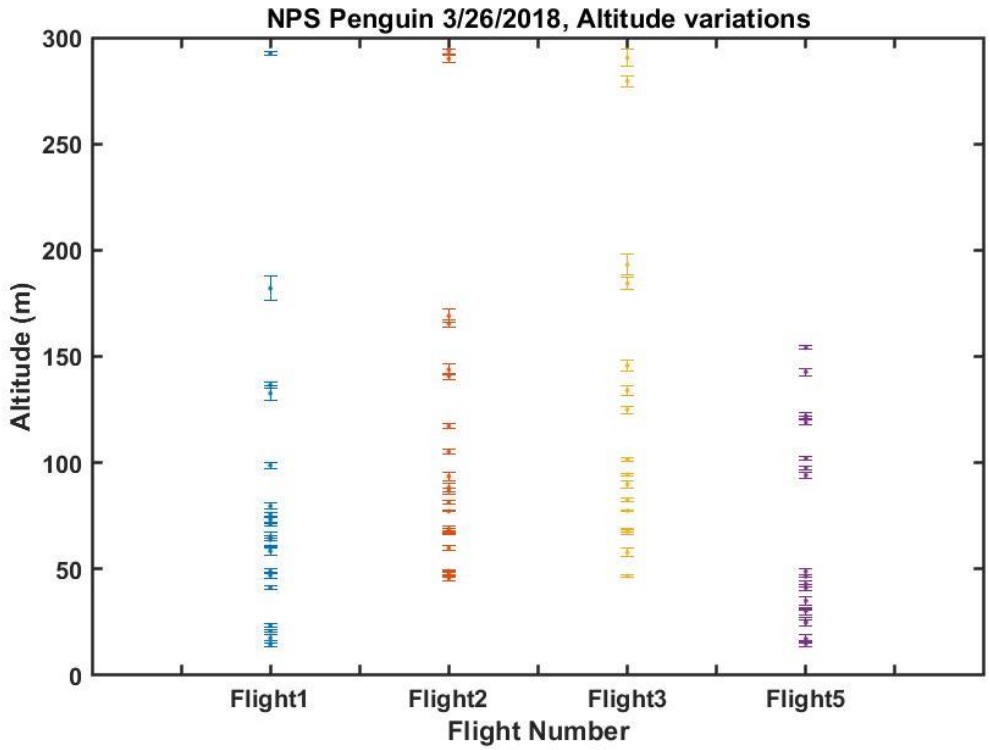

Figure 26. Mean and standard deviation of all level legs from the four good flights on 26 March 2018

Additional variability was found in the length of the clean leg cuts. Some of the leg cuts were just over a 100 m whereas others were as long as 600 m. A typical level leg is about 300-400 m in length, corresponding to 20-30 second of flight time. The airspace the Penguin was restricted to was under 900 m long. Within this span, the Penguin needed to conduct two 180 degree climbing legs with a straight and level section in between. The Penguin took additional time to adjust to level flight from the climbing turns. Also, as discussed earlier, when the Penguin flew below 50 m, it needed to dive out of the turns first to reach the lower level leg altitude before acquiring level flight characteristics. The length of all level legs of the four flights flown on 26 March 2018 can be seen in Figure 27. Table 5 gives summary of the flight characteristics for all the level legs including the mean altitude, standard deviation, leg length and flight time.

Table 5. Information of all straight level legs from all four flights on 26 March 2018

Leg #	Flight 1			Flight 2			Flight 3			Flight 5		
	z/σ_z (m)	L (m)	T (sec)	z/σ_z (m)	L (m)	T (sec)	z/σ_z (m)	L (m)	T (sec)	z/σ_z (m)	L (m)	T (sec)
1	65.3/1.9	406.2	20.2	68.7/1.6	251.1	22.5	67.7/1.5	254.6	22.2	46.5/0.63	192.1	8.8
2	71/0.55	179.9	12.6	68.1/0.96	228.1	11.1	280/2.5	496.6	23.1	43/1.4	323.2	24.8
3	64.5/0.93	144.6	7.0	294/1.2	195.1	11.1	290/4.2	241.7	19.8	30.8/0.22	97.5	4.5
4	63.7/0.52	133.0	8.3	290/1.8	194.0	17.0	193/5	452.7	24.7	41.2/1.5	256.0	22.2
5	79.7/1.5	219.7	12.2	169/3.2	547.2	33.3	184/2.9	281.3	19.7	35/1.9	212.3	18.4
6	60.5/0.35	119.9	8.6	165/1.8	416.0	30.5	134/2.4	366.1	19.6	25.4/2	406.2	18.9
7	75.8/0.81	162.2	9.2	141/1.5	573.6	36.4	146/2.5	454.2	37.5	30.3/1.8	336.0	29.1
8	73.3/1	263.1	17.5	144/2.5	505.1	38.4	125/1.7	228.8	19.1	15.9/0.4	165.3	7.3
9	293/0.67	191.5	12.3	117/1.4	314.5	19.6	94.4/0.74	264.6	12.5	24.7/1.5	256.2	23.0
10	182/5.7	305.9	26.9	93.6/2.1	561.1	33.6	102/0.83	129.8	11.8	14.9/1.1	333.5	15.4
11	133/3.5	310.2	18.4	105/1.2	244.6	19.3	82.5/0.88	342.1	15.8	17.3/1.9	554.9	40.0
12	137/1.4	331.2	27.4	86.8/1.4	388.0	20.5	89.9/1.8	401.6	33.6	48.9/1.6	376.2	21.0
13	98.8/1.3	160.2	9.5	88.4/2.2	458.7	38.4	77.5/0.46	212.9	10.5	154/0.88	220.1	10.6
14	74/2.5	218.2	20.3	77.2/0.33	264.4	14.0	67.9/0.73	448.2	22.3	143/1.7	130.5	13.3
15	58.5/2	336.8	20.0	81.4/0.87	202.7	15.1	57.8/2.2	481.5	30.8	119/0.95	229.9	11.2
16	47/1.6	315.8	25.0	67.1/1.1	321.6	19.3	46.8/0.83	246.2	13.1	122/1.7	209.5	19.1
17	48.9/1.1	334.5	21.7	67.8/1.2	280.1	19.0				121/0.63	140.1	16.3
18	41.3/0.88	314.2	23.1	59.9/1	281.0	16.2				94.1/1.4	143.8	18.7
19	23.5/0.91	131.9	10.3	47.8/1.4	262.6	15.7				102/1.1	377.2	17.0
20	17.6/1.4	281.8	19.6	49.1/0.71	136.0	9.9				102/0.81	122.7	20.1
21	14.9/1.6	451.8	32.3	45.6/1.1	480.3	28.3				97.7/0.8	137.6	19.9
22	14.7/1.4	209.7	12.9	46.8/0.63	122.1	9.5						
23	14.4/0.88	164.2	12.1									
24	20.8/0.65	186.7	12.1									

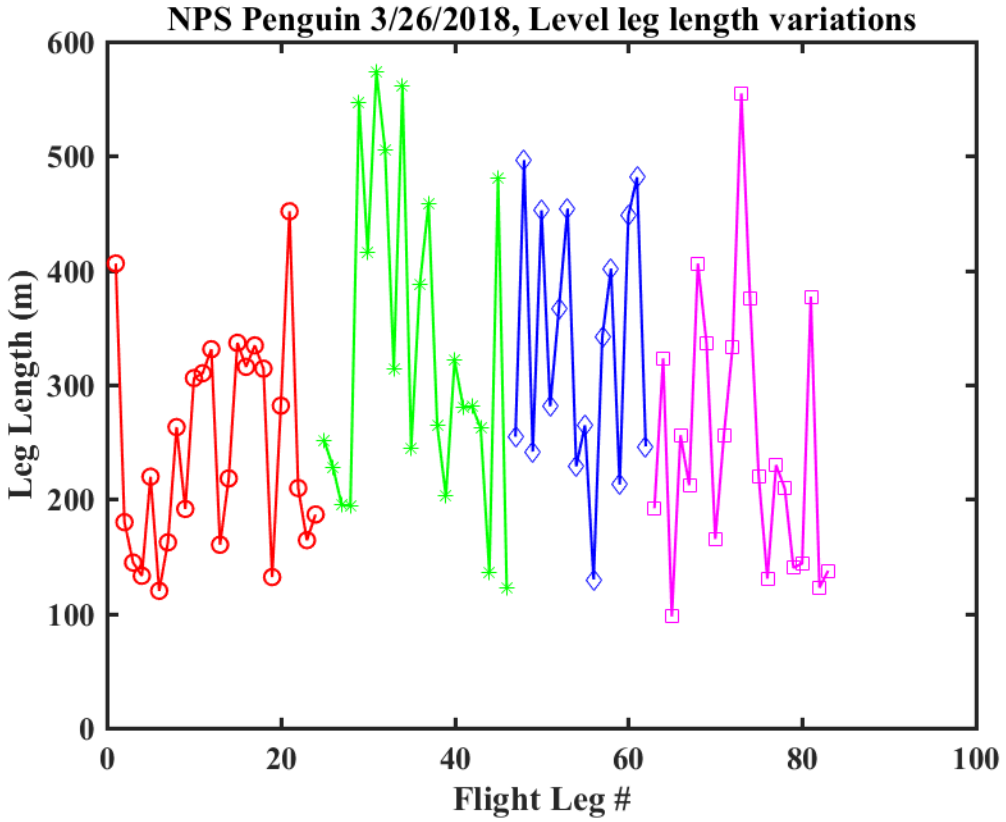

Red, green, blue, and magenta colors are for Flights 1, 2, 3, and 5, respectively.

Figure 27. Level leg length variability from all 26 March 2018 flights.

C. MEAN METEOROLOGICAL MEASUREMENTS

Fair weather conditions were observed during testing on March 26th, 2018 at the McMillian Airfield with a partly cloudy sky and light winds. This large-scale forcing produced a typical convective boundary layer over land surfaces (Stull 1988). Figure 28 shows air temperature and relative humidity from both the tower and tripod. Additionally, the tripod's soil temperature and the air-surface temperature difference are also shown in Figure 28. Temperature increased throughout the measurement period as relative humidity decreased with persistent surface warming solar radiation. The surface and air temperature difference reveal the convective nature of the sampled surface layer with its thermal instability. The largest values around noon indicate the strongest surface heating most suitable for convective development. When the temperature difference approaches zero around 1500, the surface layer becomes close to neutral (stable) near the surface.

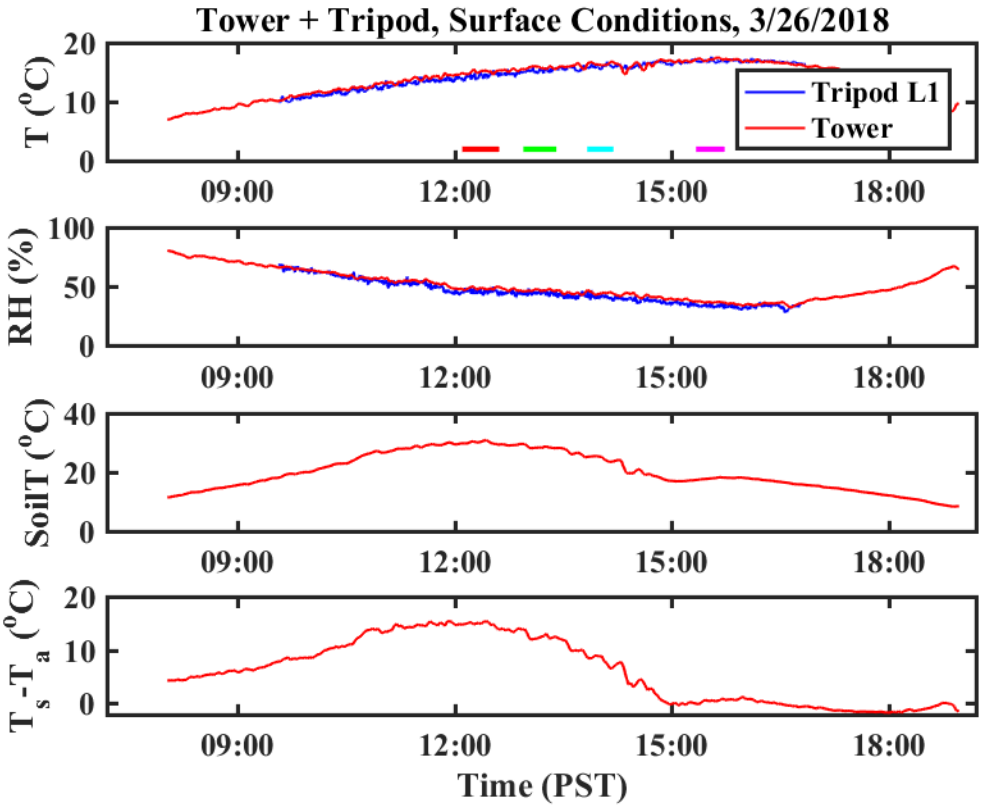

Soil temperature was also taken from the tripod mast. The lowest panel shows the difference in temperature between the surface and the air as an indicator of surface layer thermal stability.

Figure 28. Temperature and relative humidity measurements from the tripod and tower at the airfield.

Figure 29 shows the temporal variation of other meteorological conditions measured on the tripod and tower during the 26 March testing. During the sampling period, there was only a slight drop in pressure of approximately 1.5 mb. The wind speed increased to 5-7 ms^{-1} around 1500 PST from 3-4 ms^{-1} earlier while wind direction stayed mostly consistent throughout the day from the north. The stronger wind later in the day should have significant impact on boundary layer turbulence because its of contribution to generating ECE's in conjunction with buoyancy forcing.

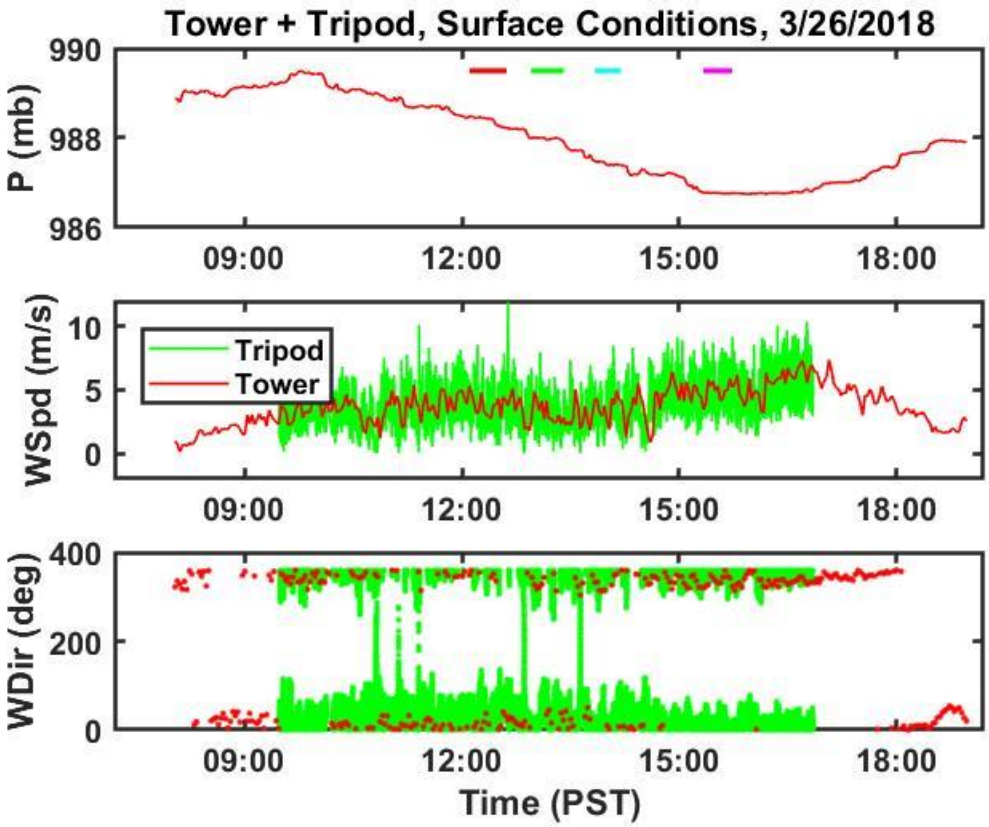

The time periods corresponding to each of the four Penguin flights are indicated by the colored thick lines on the pressure plot.

Figure 29. Mean wind speed and direction from the tripod mast and the McMillian tower.

Figure 30 shows all of the high-rate sampled wind and thermodynamic variables from the IRGASON. Increased perturbations in these variables is indicative of stronger turbulence. The increased variance in the horizontal wind components and in vertical velocity around 1500 is likely due to the increased mean wind speed.

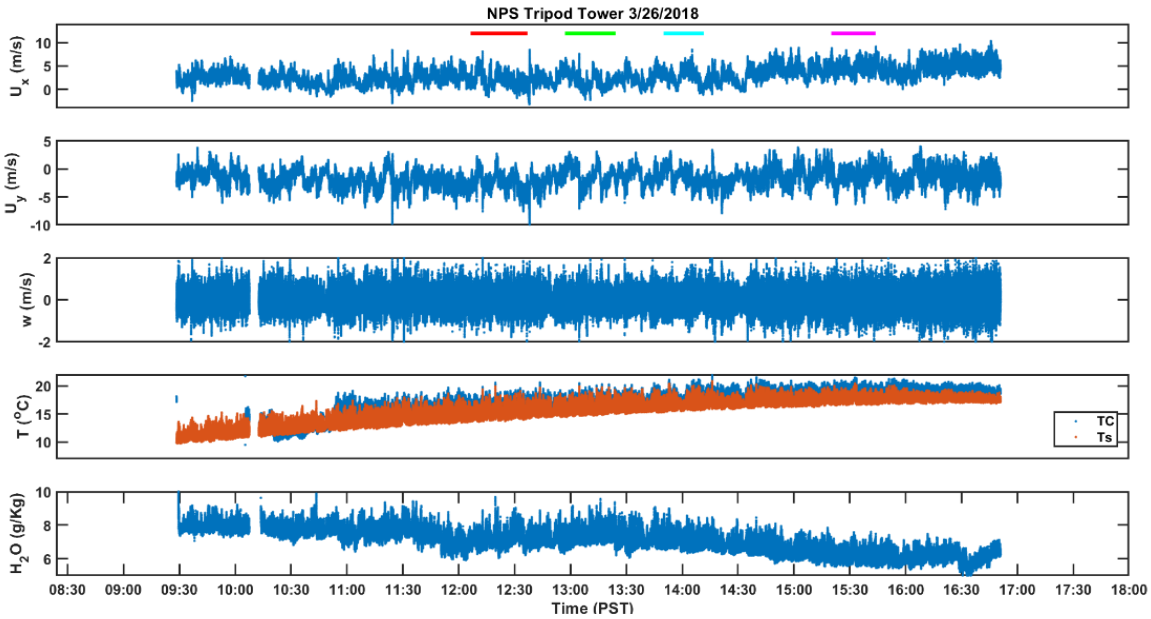

Wind speeds in the along-wind and cross-wind direction (U_x and U_y), air vertical velocity (w), temperature (Ts) and water vapor density (H2O), all from the IRGASON on the tripod mast. Tc is the temperature from the thermocouple mounted on the IRGASON. The time periods corresponding to each of the four Penguin flights are indicated by the colored thick lines on the U_x plot.

Figure 30. Tripod measured horizontal and vertical wind speeds alongside temperature and water vapor density

The composite of the mean values from all level legs of each flight forms a vertical profile as seen in Figures 31 and 32. From each of the level legs, a mean temperature was derived from the platinum thermometer. The vertical gradients shown in each profile clearly shows super-adiabatic temperature trend, indicating an unstable surface layer as expected for the daytime overland. In addition, we observed the progressively warming surface layer in response to surface temperature increase throughout the measurement period. This trend is consistent with the measurements on the tripod mast and the McMillian tower (Figures 28 and 30).

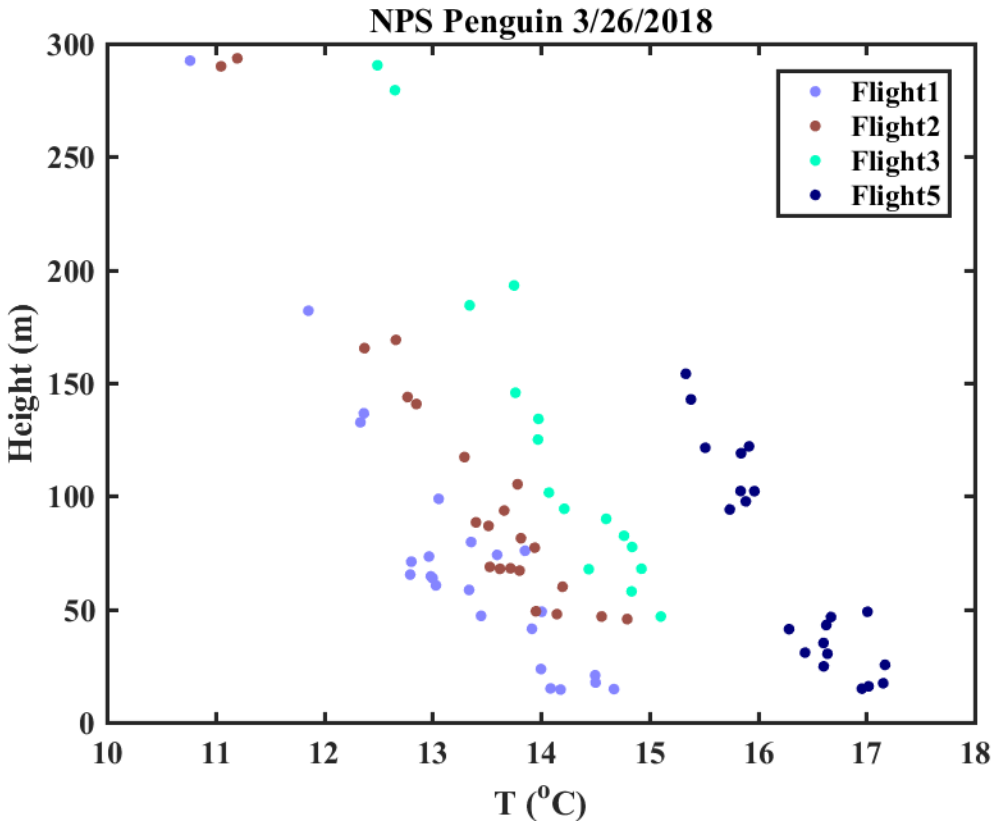

Figure 31. Temperature profiles generated by mean temperature from all level legs from each flight

Figure 32 shows the decrease of water vapor specific humidity with height in the surface layer during Flights 1, 2, and 5. Similar moisture lapse was not observed during Flight 3 as the lowest leg on this flight was much higher (~50 m). In contrast to the increasing trend of surface layer temperature, the surface layer specific humidity profile stayed relatively steady during the first three flights and decreased by about 1 gKg^{-1} during Flight 5. Such temporal variation is consistent with that shown in Figure 30 from measurements on the tripod mast. The relative humidity was measured by the onboard radiosonde and is shown in Figure 33. Apparently, the drop in specific humidity on Flight 5 was accompanied by a distinct decrease in relative humidity. A gradual decrease in relative humidity was observed during the first three flights.

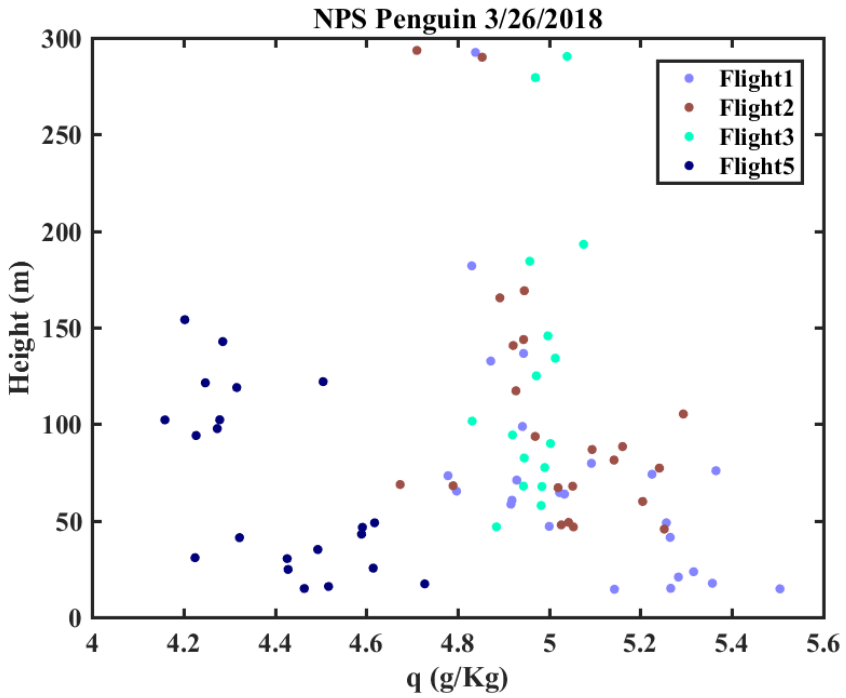

Figure 32. Same as in Figure 31, except for specific humidity

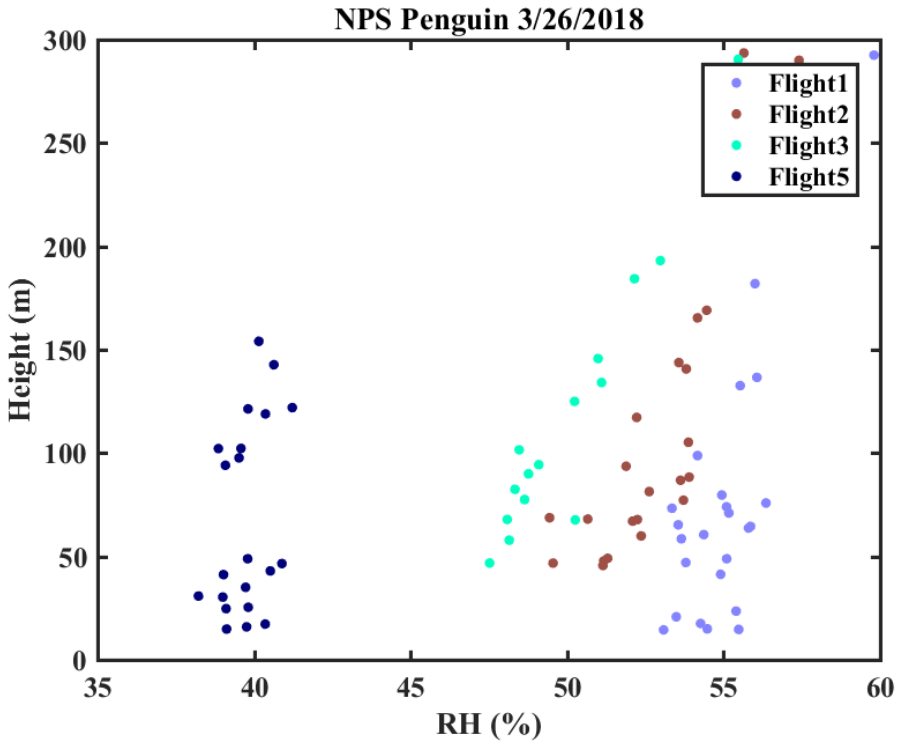

Figure 33. Same as in Figure 31, except for relative humidity.

The range of temperature perturbations collected by the Penguin varied substantially at different flight levels. Figures 34 and 35 show a clear comparison of the temperature perturbations from a sample leg at 15 m above ground to that at 68 m. As seen in Figure 28, the surface-air temperature difference is indicative of an unstable surface layer. Warm plumes form near the surface due to heating at the surface. As the warm plumes rise into the higher level, the magnitudes of perturbations are reduced due to mixing with the environment. With altitude, these plumes become weaker and broader as they entrain surrounding air, and therefore, the temperature perturbations are noticeably dampened at higher altitude.

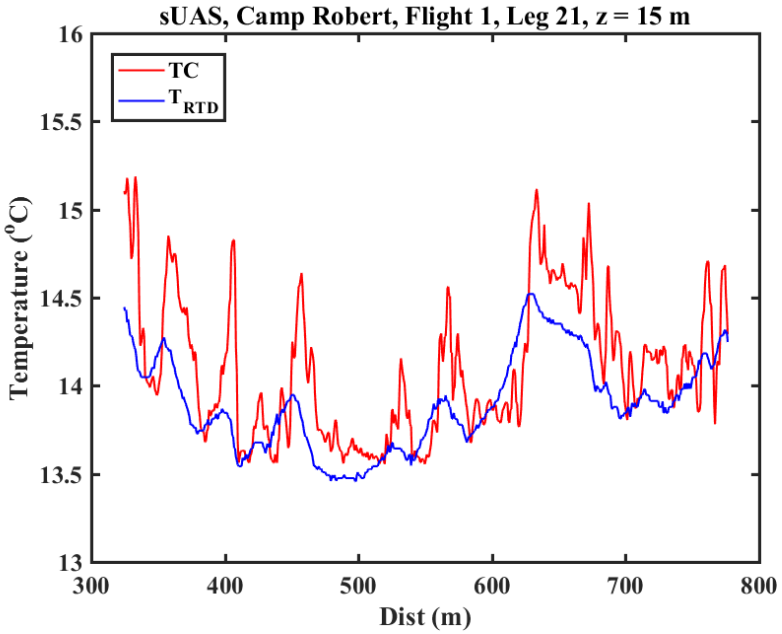

Measured by the Penguin's onboard thermocouple and platinum temperature sensor

Figure 34. Temperature perturbations at 15 m above ground

Although the thermocouple has fast response to temperature perturbations, its mean temperature tends to drift with time. As a result, a reference temperature with high absolute accuracy is needed for calibrating the thermocouple temperature to achieve absolute accuracy. The difference between the thermocouple and the reference platinum temperature sensor can be clearly identified in Figures 34 and 35. Fortunately, for the

optical turbulence applications, the temperature perturbations are key in quantifying optical turbulence. We nevertheless still include the more accurate platinum temperature sensor as part of the Penguin payload which can be used to correct for this drift for other applications.

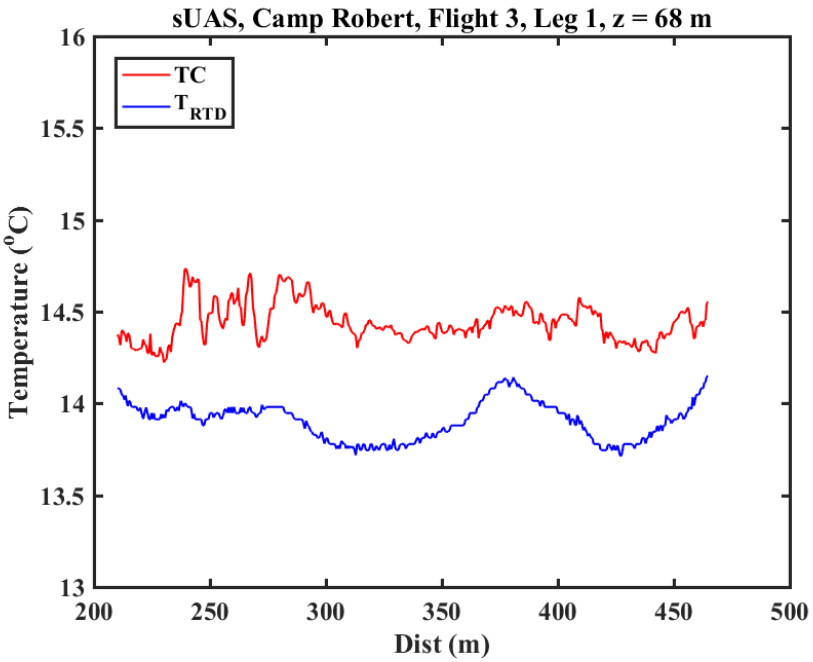

Figure 35. Same as in Figure 34, except for measurements at 68 m above ground.

The temperature perturbations are further illustrated in Figure 36, where standard deviations from both the thermocouple and platinum thermometer measurements are plotted against altitude. A dashed line is added here to help identify the values from the two sensors at the same level. It is clear that fast response thermocouple almost always reveals stronger perturbations at all levels compared to the RTD thermometer. The trend of both sensors indicates large deviations at the surface which decrease with altitude as the plumes gradually mixed with the environment.

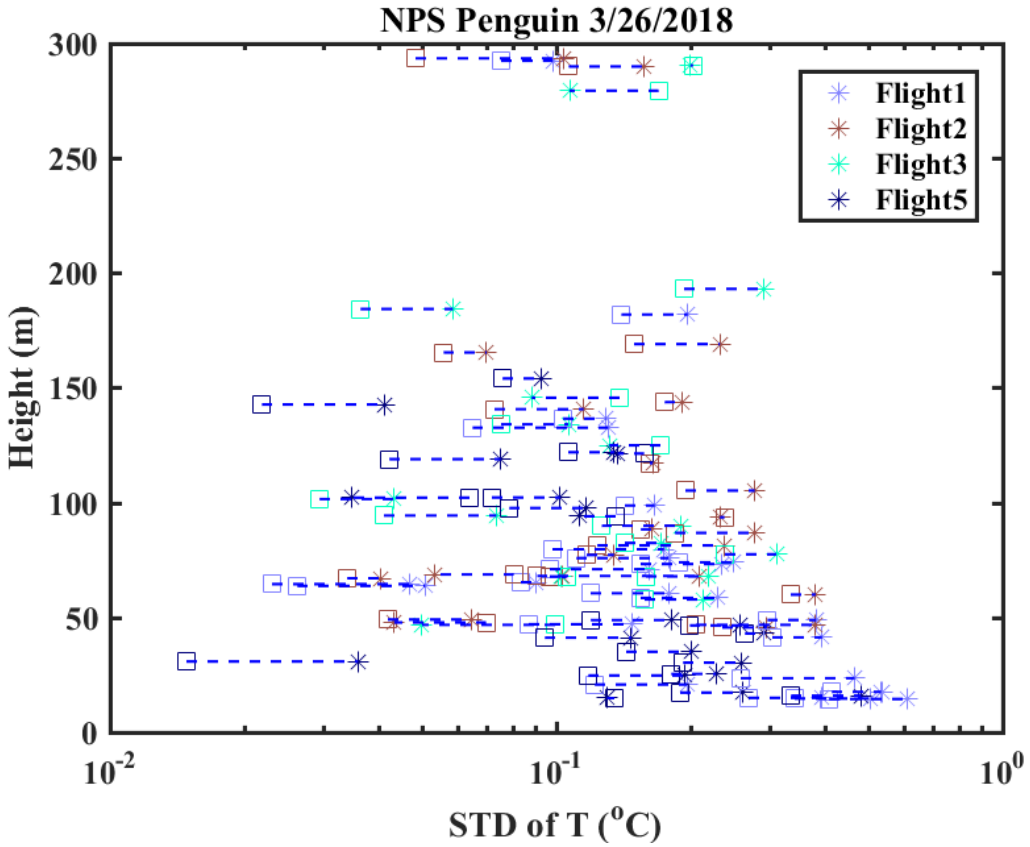

Thermocouple (stars) and the platinum thermometer (squares)

Figure 36. Standard deviations of temperatures for all flights and their variation with altitude

To further evaluate the measurements of the thermocouple, spectral analyses are performed for the level leg measurements. The energy density spectra for the same measurements in Figures 34 and 35 are shown in Figure 37 and 38. Similar to the Marina testing case, the energy density spectrum of the temperature perturbations of the thermocouple recorded by the Penguin follow the same -5/3 turbulence power law. This trend is indicative of the expected energy cascade as eddies decrease in size within the inertial subrange.

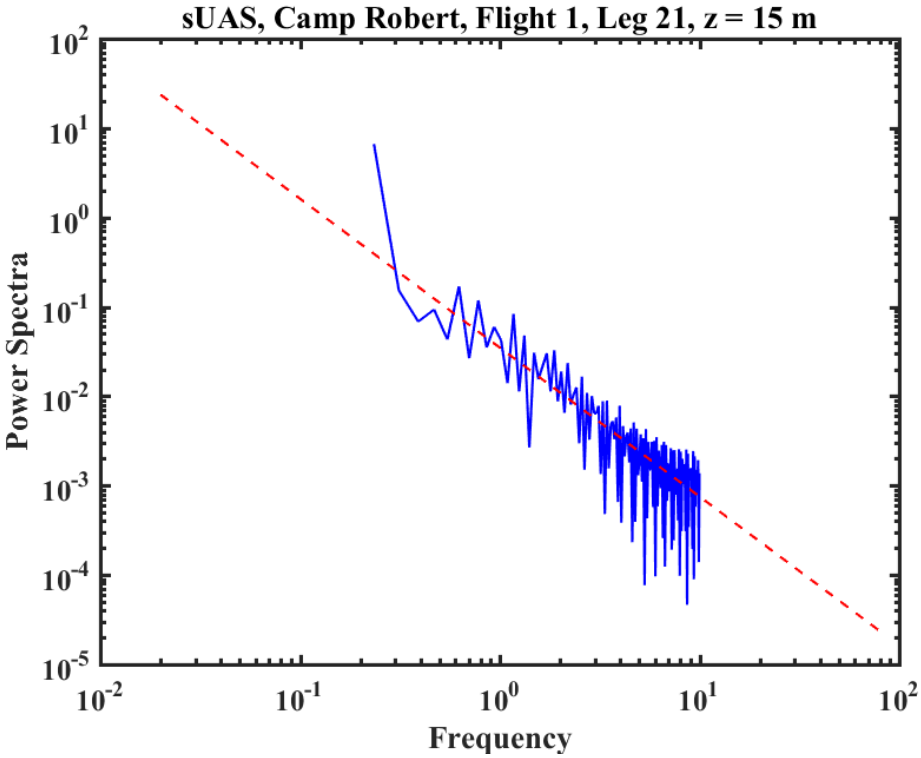

The red dash line shows the -5/3 power law as a reference.

Figure 37. The energy density spectrum of the thermocouple's temperature perturbations at 15 m.

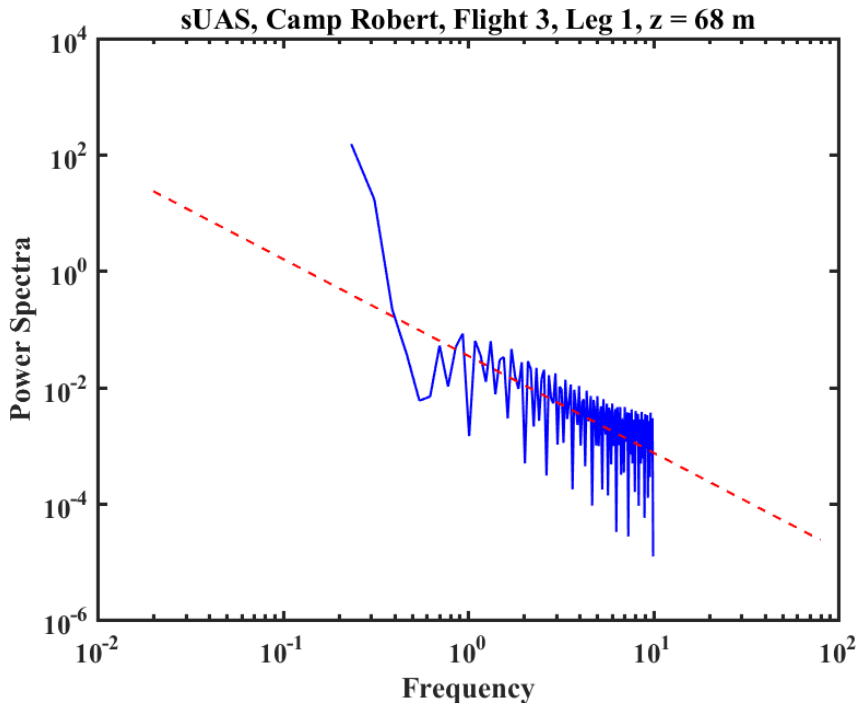

The red dash line shows the -5/3 power law as a reference.

Figure 38. Same as Figure 37, except for measurements made at 68 m above ground.

The level leg data were further processed to calculate the structure parameter for temperature C_T^2. The results for all legs from all flights are shown in Figure 39. Figure 39 does not seem to suggest strong temporal variation except near the surface. However, the Penguin measurements show significant decrease of C_T^2 with height as expected from the MOS theory.

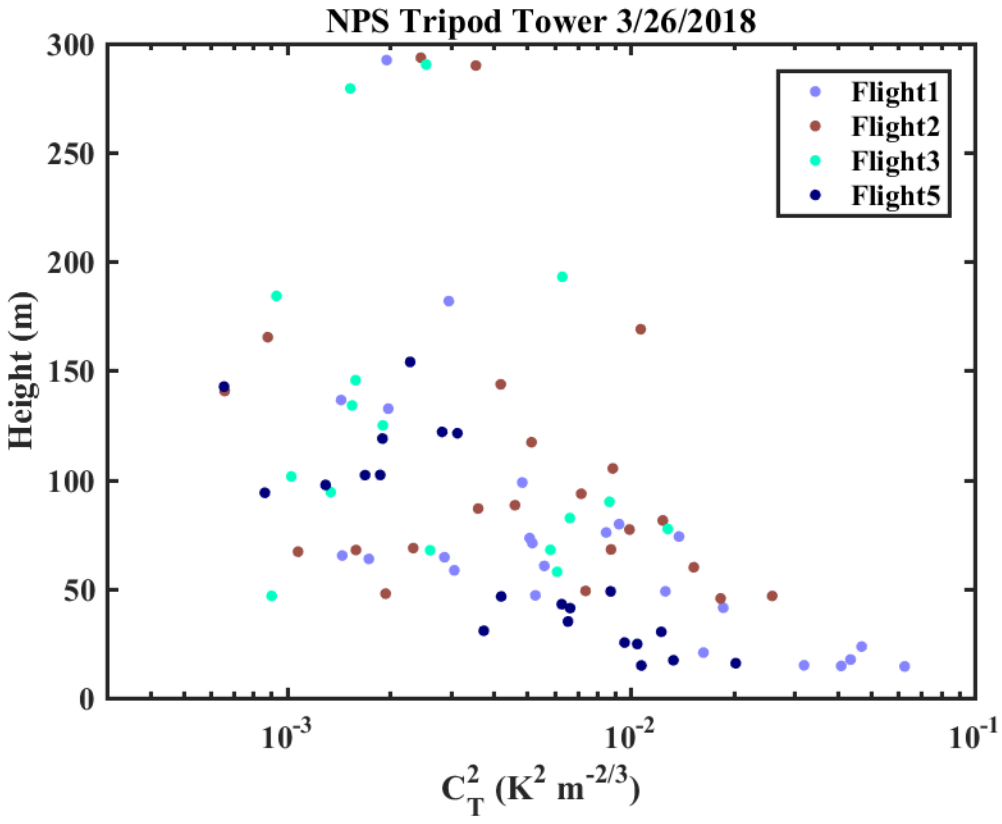

Figure 39. C_T^2 obtained from all level legs and their variation with altitude.

Figure 40 shows the C_n^2 profiles derived from the C_T^2 profile in Figure 39. Since the structure parameter for temperature, C_T^2, is the dominant component of the refractive index structure parameter, C_n^2, the trends are almost identical in Figure 40. Turbulence values of $C_n^2 = 10^{-13}$ are indications of strong turbulence as would be expected with the temperature profile and fluxes identified in the lower atmosphere.

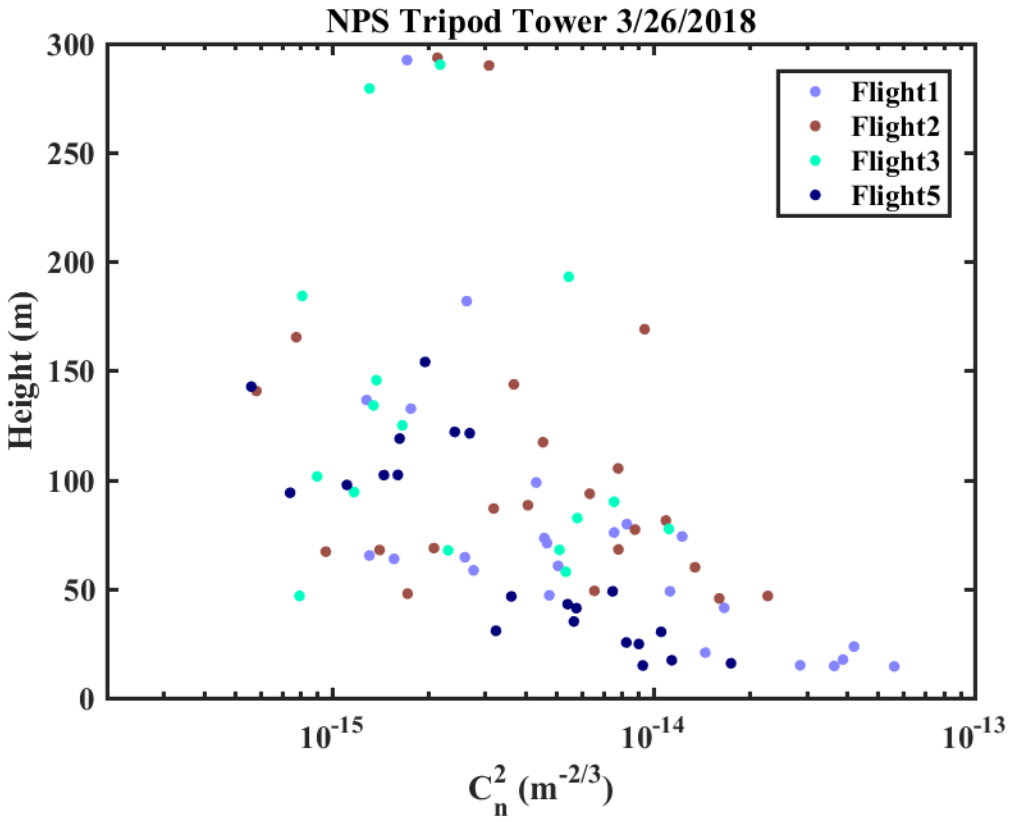

Figure 40. Same as in Figure 39, except for C_n^2.

Figure 41 shows a comparison of C_n^2, from the Penguin flights and the corresponding tripod measurement. C_T^2 vales from the tripod were generated from temperature perturbation measurements by the thermocouple mounted at 2.57 m above the surface. Based on the mean measurements from the tripod, we also derive the C_T^2 using the MOS theory in Equations (13-16) and overlay the MOS profiles on top of those from the Penguin and the tripod. As seen in Figure 41, there is a strong decreasing trend at the surface, especially during peak hours of instability towards higher C_T^2 values. We also found, that although the MOS theory indicates decrease of C_T^2 with height, its C_T^2 is almost an order of magnitude larger than those found in the Penguin's data. The Penguin measurements suggest much stronger gradient of C_T^2 that MOS theory indicates. Figure 42 gives the corresponding comparison for C_n^2 which shows similar deviation of the MOS theory from the Penguin measurements. More measurements in different atmospheric conditions should be made to further investigate these discrepancies.

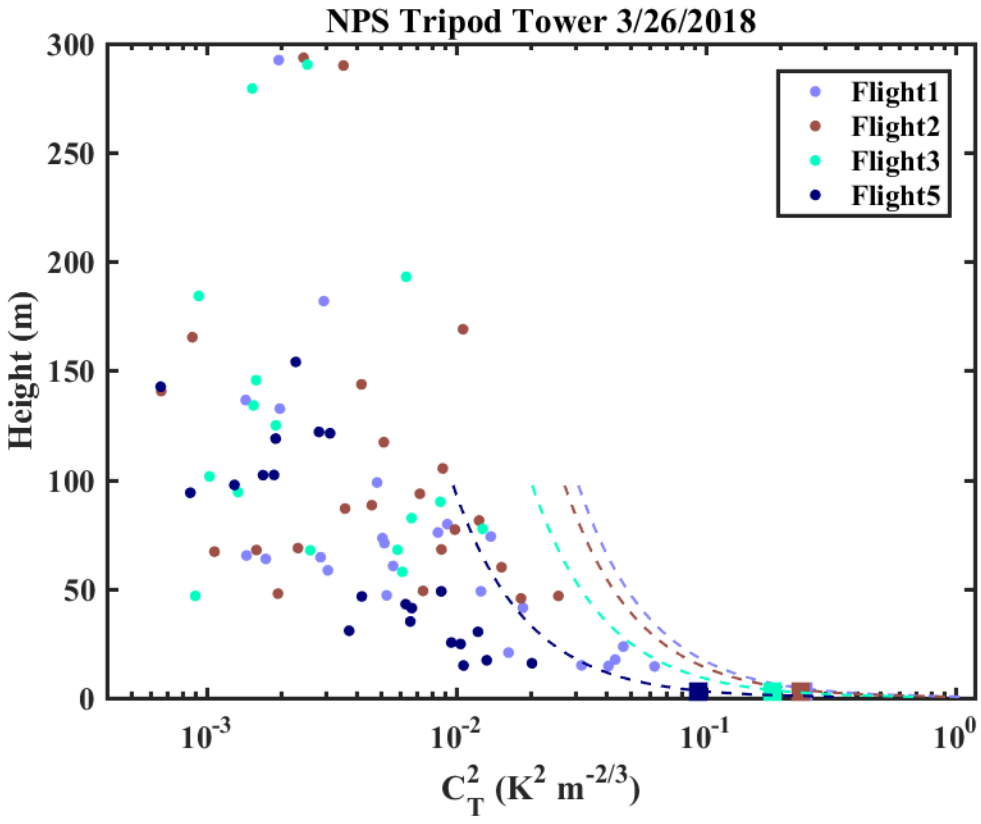

Obtained from all level legs, of the four flights with their variation with altitude

Figure 41. C_T^2 compared with tripod-based flux derived profiles and sonic anemometer temperature perturbation points.

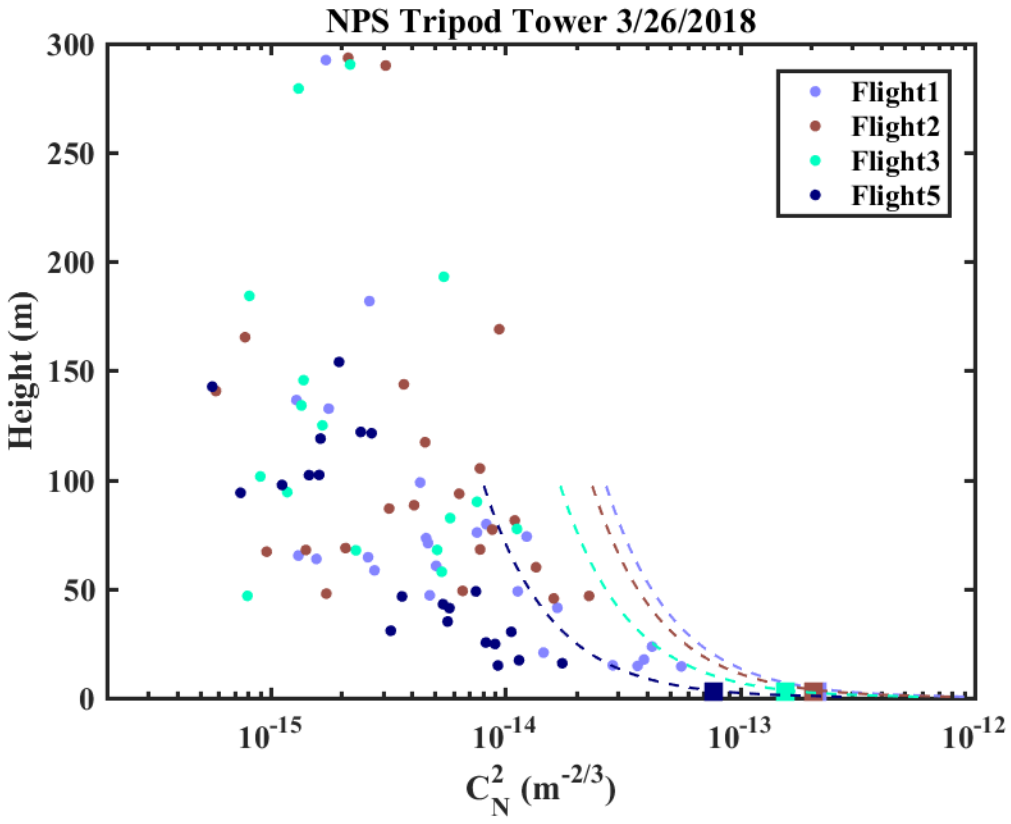

Figure 42. Same as in Figure 41, except for C_n^2.

THIS PAGE INTENTIONALLY LEFT BLANK

V. SUMMARY AND CONCLUSIONS

Improving prediction and measurement technologies for key atmospheric properties affecting electro-optical propagation is a critical effort for the U.S. Department of Defense (DoD) as it has a significant interest in current and future utilization of directed energy weapons. Understanding how the atmosphere affects electro-optical propagation is also important for improving simulation and forecast capabilities to support both directed energy weapon development and their operational use.

The objective of this thesis work was to develop and test small Unmanned Aircraft Systems (sUAS) based payloads in support of quantifying optical turbulence. Since temperature perturbations are a major factor affecting optical propagations in the atmosphere, our focus is to develop fast sampling capability for temperature. The thermocouple is our choice of the major sensor for its fast response to environmental temperature variations and for its light weight and low power requirements. A primary issue in developing a complete payload system is to digitize the thermocouple measurements with adequate data acquisition system suitable for the Penguin platform with its limits on payload weight and power consumptions. The Teensy micro-datalogging device was used for this purpose. There are three objectives for the payload development and flight testing. First, the thermocouple needed to be able to resolve small-scale perturbations in the turbulence inertial subrange. Secondly, the Teensy on the Penguin needed to match within a reasonable fmargin the industry standard data logging devices, such as the Campbell Scientific CR6 data logger. Third, the Penguin needed to conduct optical turbulence measurements over some horizontal distance to ensure representative sampling of the small turbulence eddies throughout the air column.

The payload system was first tested on the truck bed with a 3-D sonic anemometer and gas analyzer (the Campbell scientific IRGASON) setup side-by-side by the Penguin. Identical thermocouples were installed both on the Penguin logged by the Teensey and on the IRGASON logged by the CR6 datalogger. This ground testing over the tarmac proved the capability of the thermocouple payload in resolving the inertial

subrange turbulent eddies. The result provided the confidence on the Teensey datalogger marking it as a suitable data logging device for the sUAS.

In addition to the thermocouple and the RTD reference thermometers, a self-recording iMet radiosonde package was also included as the Penguin's meteorological sensor payload. The radiosonde package provides the mean temperature, humidity, and pressure of the dataset. We also took advantage of the Pixhawk autopilot system to obtain the mean wind and GPS position at a spatial resolution much better than those from the radiosonde package. The radiosonde and platinum thermometer were able to create reasonable temperature and humidity profiles generated from the level legs at multiple altitudes during each flight.

The Penguin sUAS conducted 10 flights at Camp Roberts with level legs ranging from 15 m to 300 m in altitude with soundings throughout those flight levels. The level leg lengths ranged from 100 m to 600 m with altitude variations of only a few meters. These level legs were carefully selected to ensure good quality data used in the analyses.

The final objectives of the Penguin sensor payload is to produce the vertical profiles of C_T^2 and C_n^2. Test flights at Camp Roberts resulted in reasonable meteorological and C_n^2 profiles in an unstable boundary layer with the strongest optical turbulence at the surface and decreasing with height. C_n^2 values at the surface as measured by the Penguin were approximately 10^{-14} $m^{-2/3}$ which is a reasonable estimate for the strong turbulence expected within a super adiabatic surface layer. The values also compared well with the tripod measured corresponding values taking into consideration of the strong vertical gradient near the surface. These results validate the capability of the sUAS platform utilizing the low cost, lightweight and low-power consumption thermocouple probe to detect eddies within the inertial sub-range. Further comparisons of the Penguin measured C_n^2 and those expected from MOS theory suggest strong gradients in C_n^2 from the observations.

A. FUTURE WORK AND RECOMMENDATIONS

Measurements by the sUAS Penguin provide a valuable dataset to prove the capabilities of the thermocouple and sUAS platform in detecting optical turbulence

within the lower atmosphere. One of the unforeseen challenges encountered was with the flight characteristics of the Penguin. Maintaining a consistent altitude after the Penguin hit its intended waypoints was a challenge. The aircraft would either continue to climb or dive instead of maintaining the altitude of the last (or its next waypoint) on the level legs. This can be corrected by tuning both the waypoints and the flight control responses onboard the autopilot. With more consistent altitude control, the level leg cuts would be longer since variability could be reduced. Additionally, flying the Penguin at another location where the flight area was larger would reduce the effect of temporal and spatial variabilities within the surface layer resulting in more precise statistics.

The use of the sUAS platform to explore the effects of the atmosphere on directed energy weapons is in its infancy and has much more potential. Higher sampling rate fine-wire thermometers are available and can be potentially integrated into the Penguin's sensor payload. These fine wire thermometers allow for the entire inertial sub-range (down to the millimeter) to be measured which would further improve the quality of the structure parameter for temperature. Our flights were limited to mild weather conditions over inland environments. Conducting flights along the coast or out at sea in various meteorological conditions would help improve the understanding of the optical turbulence in the maritime environment, which is especially helpful for the U.S. Navy. Three-dimensional turbulence sensors are also desirable as part of the Penguin sensor payload to augment the current sampling capability. In addition, using a quadrotor and/or developing autonomous launch and landing capabilities for the fixed-wing sUAS would further allow for improved functionality in the operational environment, especially out at sea. However, issues associated with flow distortion and flight regulations/authorizations need to be resolved. Finally, flying a swarm of sUASs simultaneously could allow for huge swaths of the lower atmosphere to be sampled with increased precision in an even shorter time frame. Incorporating the Penguin measurements into operational forecast models should also enhance the Navy's capability in forecasting the battlespace environment.

THIS PAGE INTENTIONALLY LEFT BLANK

LIST OF REFERENCES

Andreas, E. L. (1988). Estimating Cn2 over snow and sea ice from meteorological quantities. https://doi.org.10.1117/12.945784

Andrews, L. C. (2007). *Field guide to atmospheric optics*. Bellingham, Wash: SPIE.

Atmospheric propagation of high-energy laser beams. (n.d.). Retrieved June 7, 2018, from https://www.nrl.navy.mil/ppd/atmo-prop

Burger, L., Litvin, I. A., & Forbes, A. (2008). Simulating atmospheric turbulence using a phase-only spatial light modulator. *South African Journal of Science, 104*(3-4), 129–134. Retrieved June 08, 2018, from http://www.scielo.org.za/scielo.php?script=sci_arttext&pid=S0038-23532008000200011&lng=en&tlng=en

Center for Directed Energy (CDE). (n.d.). Retrieved June 08, 2018 from https://www.afit.edu/cde/page.cfm?page=331&tabname=Tab5A

Dias, N. L., Gonçalves, J. E., Freire, L. S., Hasegawa, T., & Malheiros, A. L. (2012). Obtaining potential virtual temperature profiles, entrainment fluxes, and spectra from mini unmanned aerial vehicle data. *Boundary-Layer Meteorology,145*(1), 93–111. https://doi.org.10.1007/s10546-011-9693-2

Edson, J. B., & Fairall, C. W. (1998). Similarity relationships in the marine atmospheric surface layer for terms in the TKE and scalar variance budgets. *Journal of the Atmospheric Sciences, 55*(13), 2311–2328. https://doi.org.10.1175/1520-0469(1998)0552.0.co

Elston, J., Argrow, B., Stachura, M., Weibel, D., Lawrence, D., & Pope, D. (2015). Overview of small fixed-wing unmanned aircraft for meteorological sampling. *Journal of Atmospheric and Oceanic Technology,32*(1), 97–115. https://doi.org.10.1175/jtech-d-13-00236.1

Foken, T. (2006). 50 years of the Monin–Obukhov similarity theory. *Boundary-Layer Meteorology,119*(3), 431–447. https://doi.org.10.1007/s10546-006-9048-6

Frederickson, P. A. (2015). Further improvements and validation for the Navy atmospheric vertical surface layer model (NAVSLaM). *2015 USNC-URSI Radio Science Meeting (Joint with AP-S Symposium).* https://doi.org.10.1109/usnc-ursi.2015.7303526

FW1 - Type E Fine-Wire Thermocouple. (n.d.). Retrieved June 7, 2018, from https://www.campbellsci.com/fw1

Kaimal, J. C., Wyngaard, J. C., Haugen, D. A., Coté, O. R., Izumi, Y., Caughey, S. J., & Readings, C. J. (1976). Turbulence structure in the convective boundary layer. *Journal of the Atmospheric Sciences, 33*(11), 2152–2169. https://doi.org/10.1175/1520-0469

Lawson, J. K., & Carrano, C. J. (2006). Using historic models of Cn2 to predict r0 and regimes affected by atmospheric turbulence for horizontal, slant, and topological paths. *Atmospheric Optical Modeling, Measurement, and Simulation II*. https://doi.org.10.1117/12.679108

Nelson, D. H., Walters, D. L., Mackerrow, E. P., Schmitt, M. J., Quick, C. R., Porch, W. M., & Petrin, R. R. (2000). Wave optics simulation of atmospheric turbulence and reflective speckle effects in CO2 lidar. *Applied Optics,39*(12), 1857. https://doi.org.10.1364/ao.39.001857

Pike, J. (n.d.). McMillan Airfield. Retrieved from https://www.globalsecurity.org/military/facility/mcmillan.htm

Sprangle, P., Penano, J. R., & Hafizi, B. (2005). Optimum wavelength and power for efficient laser propagation in various atmospheric environments (Vol. 2). Retrieved June 6, 2018, from http://www.dtic.mil/dtic/tr/fulltext/u2/a441474

Stull, R. B. (1988). Atmospheric boundary layer. Retrieved June 7, 2018, from http://glossary.ametsoc.org/wiki/Atmospheric_boundary_layer

Szoeke, S. P., Skyllingstad, E. D., Zuidema, P., & Chandra, A. S. (2017). Cold pools and their influence on the tropical marine boundary layer. *Journal of the Atmospheric Sciences,74(*4), 1149-1168. https://doi.org/10.1175/jas-d-16-0264.1

Tatarskii, V. I. (1971). *The effects of the turbulent atmosphere on wave propagation.* Springfield, VA: Israel Program for Scientific Translations.

Wagner, D. (n.d.). Intuition vs. Snell's Law. Retrieved June 7, 2018, from https://www.rpi.edu/dept/phys/ScIT/InformationTransfer/reflrefr/rr_content/refraction_35a.html

INITIAL DISTRIBUTION LIST

1. Defense Technical Information Center
   Ft. Belvoir, Virginia

2. Dudley Knox Library
   Naval Postgraduate School
   Monterey, California